

## Article

# Post-buckling Partial Similitude Scaled Model for Stiffened Cylinders under Axial Compression by Energy Method

Wei Yu <sup>1,2,\*</sup> , Siyu Du <sup>1</sup>, Wanxu Zhu <sup>1,2</sup> and Chuntao Zhang <sup>3</sup> 

<sup>1</sup> College of Civil Engineering and Architecture, Guilin University of Technology, Qixing District, Guilin 541004, China

<sup>2</sup> Guangxi Key Laboratory of New Energy and Building Energy Saving, Qixing District, Guilin 541004, China

<sup>3</sup> School of Civil Engineering and Architecture, Southwest University of Science and Technology, Fucheng District, Mianyang 621010, China

\* Correspondence: yuwei3601@163.com

**Abstract:** Considering the geometric nonlinearity and geometric imperfection of stiffened cylinders, the generalized similitude conditions and scaling laws for axial compression post-buckling are established by applying the similitude transformation to the total energy of the structure. The post-buckling similarity of stiffened cylinders is numerically analyzed, and scale laws, through innovative application of the stiffness formulas and deformation scale factor. Based on three type geometrical imperfections, the effects of radius to effective thickness ratios, stiffened cross-sections, boundary conditions and imperfection coefficients are investigated by post-buckling partial similarity simulation of stiffened cylinders under axial compression. The results show that the partial similarity can be well realized by changing other parameters or selecting a model with a similar Poisson's ratio for the prototypical material on the premise of invariant stiffness scale factors. Partial similarity simulation of axial compression post-buckling of stiffened cylinders is not affected by radius to effective thickness ratios (23.76–268.95), classical simply supported and fixed support boundary conditions, rectangular or T-type stiffened cross-sections and three type of geometric imperfections.

**Keywords:** scaling law; post-buckling; stiffened cylinder; geometric nonlinear; energy method



**Citation:** Yu, W.; Du, S.; Zhu, W.; Zhang, C. Post-buckling Partial Similitude Scaled Model for Stiffened Cylinders under Axial Compression by Energy Method. *Buildings* **2022**, *12*, 2163. <https://doi.org/10.3390/buildings12122163>

Academic Editor: Mohamed K. Ismail

Received: 9 October 2022

Accepted: 1 December 2022

Published: 7 December 2022

**Publisher's Note:** MDPI stays neutral with regard to jurisdictional claims in published maps and institutional affiliations.



**Copyright:** © 2022 by the authors. Licensee MDPI, Basel, Switzerland. This article is an open access article distributed under the terms and conditions of the Creative Commons Attribution (CC BY) license (<https://creativecommons.org/licenses/by/4.0/>).

## 1. Introduction

The structural behavior of stiffened cylinders subjected to axial compression is characterized by buckling failure. The typical structure used by practical application in engineering such as gasholders is presented in Figure 1 [1]. Due to the limitations of experimental conditions and funds, it is impossible to conduct a large number of prototypical experiments on large and medium stiffened shells. Usually, the buckling bearing capacity of the prototype is predicted by extrapolating and empirically estimating the experimental results from scale models. Therefore, it is necessary to investigate the design method and buckling laws of scale models of stiffened shells in model tests to gain a reasonable understanding of both the buckling properties and the design of the prototype.

Many achievements have been obtained based on analytical approaches to similitude and scaling laws for buckling of plates and shells. The dimensional analysis technique was first applied to design scale models and it is a general method for structural similitude. Ezra [2] researched the buckling properties of scale models of a shell subjected to impact loads. Morgen [3] studied linear buckling of the orthogonal isotropic cylindrical shell with a combination of internal and non-axisymmetric loads. These studies showed that the dimensional analysis method can effectively establish important scale parameters and can also be used to develop other similitude-scaling relationships, especially in the case of many variables. Models of the spherical-ring-cone composite shell were designed by Huang [4], based on the similar invariant existence theorem, dimensional analysis theorem, and similar uniqueness theorem, and buckling experiments were performed on scale models using the

dimensionless geometric parameters. The theoretical buckling load is 14.2% smaller than the test result, and the reason for the discrepancy was given by the author.



**Figure 1.** Gas holder used in a practical engineering application.

A direct method was studied by using the similarity invariance of the solution of shell governing equations. Rezaeepazhand and Simites [5–8] researched partial scale models for linear buckling of laminated plates and cylinders under combined loads. The results showed that partial similarity could be achieved by changing the number of layers, the sequence of layers and the geometric dimensions of the laminated plates and cylinders based on structural similarity, a partial similarity model with an isotropic material that can predict the buckling load by selecting the radius scaling factor  $R_m$  as the design variable. The buckling properties of the prototype can be predicted by the results of partial similarity models with certain types of fiber composite materials.

The similarity transformation analysis method was explored on the governing differential equations of the structural system. Rezaeepazhand and Simites [9,10] studied the buckling scale laws for orthogonal laminated plates with uniaxial compression and shear loads, and the effects of the number of layers, material properties, and geometric dimensions were investigated. The results showed that partial similarity models with changes of layer number, material properties, and geometric size can predict the prototypical buckling properties. The partial similarity model with isotropic materials can also predict the buckling load of the prototype via selection of  $R_m$  as the design variable. Frostig and Simites [11] investigated similarity simulation of the linear buckling and strength of sandwich plates with a geometric imperfection. The results showed that the linear buckling similarity simulation could be well realized. However, the error between the strength responses of the partial similarity models with geometric imperfections and the results of the prototype was approximately 50%. Partial scaling similarities for linear buckling of laminated plates and cylinders subjected to single axial compression or combined loads were studied by Ungbhakorn and Singhatanadgid [12–15]. The results showed that partial similarity models with different layering order, layer number, material properties, and the same arbitrary boundary conditions as the prototype can be used to predict the buckling properties of the prototype based on the scaling laws. Rezaeepazhand and Wisnom [16] reported that the prototypical buckling properties of delaminated orthogonal beam-plates can be well predicted by distorted scale models with a different depth, size, and number of delamination. Shokrieh and Askari [17] proposed a continuous similarity method to study linear buckling simulation of laminate plates with impact damage based on the same material and lamination sequence between the model and prototype.

A laboratory-scale composite cylinder test article with imperfections designed according to nondimensionalized anisotropic cylinder buckling equations was investigated by simulation and testing [18,19]. The two pre-test simulations showed excellent agreement

with the results of the test at NASA Langley Research Center. However, with both measured and loading imperfections considered, the post-test simulations substantially did not affect the buckling load. The research indicates that directly measured imperfections can play a key role in the development of less conservative knockdown factors for future composite launch vehicle structures.

Using the nondimensional buckling governing equations, an analytical scaling methodology for sandwich composite cylinders under axial compression was presented by Balbin and Bisagni [20]. The methodology was used to develop scale models for reproducing a similar buckling response to the prototype. The results showed that both the prototype and scale models buckled similarly, when the nondimensional stiffness was matched between the different scaled models. The limitations of the methodology were discussed, and the reason is a result of neglecting the transverse shear and the flexural anisotropy compliance.

The challenge is to develop representative buckling-critical scale test samples. The design methodology for full-scale composite cylinder test-articles was validated by full-scale testing [21]. The test-article designs were generated and then down-selected by using simple closed-form failure calculations and the nondimensional significant design-space parameters. A large pool of possible subscale test-article designs was evaluated to predict the global buckling failure mode using higher-fidelity finite element analysis. It was discovered that the predicted closed-form buckling loads matched well the finite element results, but that the predicted strains at buckling differed significantly. This difference leads to slight redesigns of partial test articles. The selected designs are given by buckling-response predictions from the closed-form analyses and geometrically nonlinear finite element analyses with geometric imperfections. The proposed iterative design process is used to develop buckling-critical specimens in the design space of interest.

The energy method of applying the similitude transformation to the total energy of the structure system was performed. This method has been applied to study linear elastic beams, static deformation for scale models of plates [22], natural vibration scale models of plates and laminated hyperbolic shallow shells [22,23], static deformation for scale models of a linear elastic two-dimensional frame with changing material and cross-section [24], a static deformation for scale models of material nonlinear elastic beam with the same material as the prototype [24], prestressed vibration and buckling of densely stiffened circular cylindrical panels [1], axial compression post-buckling similitude model of densely stiffened cylinders with dimple imperfections [25], and structural similitude for nonlinear buckling of discrete orthogonally stiffened cylinders subjected to axial compression or external pressure [26,27]. Based on the strain energy release rate approach and the principle of conservation of energy in the linear elastic fracture mechanics framework, the structural similarity for the static deflection and slope problem of a rectangular cross-section cracked beam with elastic support was investigated [28]. The energy similitude correction method was proposed to solve free vibration high-precision similitude of aluminum alloy cylinders [29], laminated composite cylinders [30], FG porous plates [31], functionally graded material cylinders [32].

Based on the geometric imperfection function of welded stiffened cylinders, post-buckling analysis of the structure was performed by Hilburger [33–35] using the fine finite element model (FEM) and verification by scale model tests and prototype tests. The new reduction factor for the buckling load can be determined by this method without a large number of tests on large diameter stiffened cylinders. Local buckling of the skin can be prevented by reducing the spacing of longitudinal and ring stiffeners in the modified design of the model. Additionally, the constant cross-sectional area of the structure was maintained by adjusting the thickness of the longitudinal and ring reinforcement. However, a detailed design basis and the buckling scale laws of scale models were not given.

The imperfection sensitivity of a 4.5 m diameter isogrid stiffened cylinder under axial compression was investigated numerically and experimentally [36]. The NASA SP-8007 measured imperfection, and several types of assumed imperfections, such as eigenmode-shape imperfection and dimple-shape imperfections, were implemented in finite element

models for predicting the knockdown factors (KDFs), respectively. Then, the buckling test of this full-scale stiffened shell subjected to axial compression was conducted to validate the above numerical approaches. It can be shown that the KDF predicted by the worst multiple perturbation load approach (WMPLA) agreed well with the test results, while the ones predicted by NASA SP-8007 and eigenmode-shape imperfection are extremely conservative. In addition, the measured and other assumed imperfections are risky, because these methods over-estimate the actual load-bearing capacity. Finally, it can be found that the WMPLA is an efficient and potential approach to predicting the improved KDFs in the design stages of future launch vehicles.

The development of new analysis-based shell KDFs for modern integrally stiffened metallic cylinders has been presented [37]. These new KDFs were investigated according to experimentally validated high-fidelity finite element analyses including the effects of geometric and loading imperfections, stiffener longitudinal welds, pattern orthotropy, and combined mechanical and internal pressure loads. Then, these developed factors can be tailored to improve as the design matures during the design cycle. The derivation of the new analysis-based KDFs was introduced herein from which a hierarchy of KDFs had been developed for different levels of design fidelity. Selected KDFs of orthogrid-stiffened cylinders under uniform axial compression and combined internal pressure and axial compression were investigated in a simulated design cycle to explain the use of the new factors. In addition, using a high-fidelity finite element model, the resulting cylinder design was analyzed to verify these predicted buckling loads and new analysis-based KDFs. The results have shown that the new KDFs can be used to generate robust preliminary designs considering relevant characteristic imperfections and design features. In a mathematically consistent manner, these KDFs can be improved according to the design cycle and corresponding mature design tools.

Stiffened shells are viewed as orthogonal anisotropic shells based on the smeared stiffener theory. The characteristics of the four main methods for studying shell buckling scale models are as follows. The dimensional analysis method is more suitable for the case of fewer structural design parameters, and this method is more complicated when the structural design parameters are more numerous. The similitude method applied to the solution of the governing equations must first assume the displacement function, and closed-form or approximate solutions must be obtained before applying the similitude transformation. If the structure is more complicated or the displacement function is difficult to express, this method is restricted and complicated for selection of scale laws, and the advantage of the similitude method is underused. The considered similarity conditions are far fewer than the design variables in the similitude method applied to the differential equations, which makes it convenient for partial similitude simulation. However, the governing differential equations of stiffened shells can be obtained via the energy function of the structure, and thus, this method does not appear to be sufficiently direct and convenient. Compared with the previous three methods, the energy method applying the similitude transformation to the total energy is a relatively new approach that offers the advantages of direct and simple analysis, and the similitude conditions are not affected by boundary conditions.

To meet the need for scale model tests of large stiffened cylinders, the post-buckling scaling laws of the cylinders under axial compression are improved and developed according to the structural and mechanical properties. Considering the stiffness parameter formulas and deformation scaling factor, the generalized similarity conditions and scaling laws for post-buckling of stiffened cylinders under axial compression are established by the energy method based on the Donnell nonlinear geometric equation with initial geometric imperfections. First, the reliability and correctness of the finite element analysis is verified by the literature on post-buckling of stiffened cylinders. Then, post-buckling partial similarities under axial compression are investigated for stiffened cylinders with different geometric imperfections, radius to effective thickness ratios, boundary conditions, and stiffened cross-sections.

## 2. Generalized Similitude Conditions and Scaling Laws for Post-Buckling of Stiffened Cylinders under Axial Compression

The relationship between the total energy of two similar structures of the stiffened cylindrical shell model and the prototype can be expressed as shown [23]:

$$\Pi_p(X_{pi}) = \psi(C_i)\Pi_m(X_{mi}) \quad (1)$$

where  $\Pi$  is the total energy of the system;  $X_{pi}$  and  $X_{mi}$  ( $i = 1, 2, \dots, n$ ) are geometric and physical parameters of the prototype and model, respectively; and  $\psi(C_i)$  ( $i = 1, 2, \dots, n$ ) are the transfer functions of two similar structural parameters.

The energy functional of stiffened cylinders can be expressed as follows:

$$\Pi = U + U_L \quad (2)$$

where  $U$ , and  $U_L$  are, respectively, the strain energy and the work produced by external forces.

Based on the smeared stiffener theory, the expressions for force and moment of stiffened cylinders are written as shown [38]:

$$\begin{aligned} N_x &= A_{11}\varepsilon_x + A_{12}\varepsilon_y + B_{11}\chi_x \\ N_y &= A_{12}\varepsilon_x + A_{22}\varepsilon_y + B_{22}\chi_y \\ N_{xy} &= A_{66}\gamma_{xy} \\ M_x &= B_{11}\varepsilon_x + D_{11}\chi_x + D_{12}\chi_y \\ M_y &= B_{22}\varepsilon_y + D_{12}\chi_x + D_{22}\chi_y \\ M_{xy} &= D_{66}\chi_{xy} \end{aligned} \quad (3)$$

where the expressions of stiffness parameters  $A_{ij}$ ,  $B_{ij}$ , and  $D_{ij}$  are given as follows:

$$\begin{aligned} A_{11} &= B + \frac{E_s A_s}{d_s}, \quad A_{12} = \mu B, \quad A_{22} = B + \frac{E_r A_r}{d_r}, \quad A_{66} = \frac{1-\mu}{2} B, \\ B_{11} &= e_s \frac{E_s A_s}{d_s}, \quad B_{22} = e_r \frac{E_r A_r}{d_r}, \\ D_{11} &= D + \frac{E_s I_s}{d_s}, \quad D_{12} = \mu D, \quad D_{22} = D + \frac{E_r I_r}{d_r}, \quad D_{66} = D(1-\mu) + \frac{1}{2} \left( \frac{G_s J_s}{d_s} + \frac{G_r J_r}{d_r} \right). \end{aligned} \quad (4)$$

where

$$B = \frac{Et}{1-\mu^2}, \quad D = \frac{Et^3}{12(1-\mu^2)}, \quad J_s = \frac{1}{3}(b_{fs}t_{fs}^3 + h_{ws}t_{ws}^3), \quad J_r = \frac{1}{3}(b_{fr}t_{fr}^3 + h_{wr}t_{wr}^3). \quad (5)$$

where  $B$  and  $D$  are the extensional rigidity and the bending rigidity, respectively, and  $t$  is the thickness of the skin. Subscripts  $s$  and  $r$  denote the stringers and rings, respectively, and subscripts  $f$  and  $w$  denote the flange and web of the stiffeners, respectively.  $E_s$  and  $E_r$  are the elastic modulus of the stringers and rings, respectively,  $A_s$  and  $A_r$  denote the cross-sectional areas of the stringer and ring, respectively,  $I_s$  and  $I_r$  denote the moments of inertia for cross-sections of the stringer and ring relative to the shell middle surface, respectively, and  $J_s$  and  $J_r$  denote the torsional constants of the stringer and ring, respectively. The length and thickness of the stringer flange and web are, respectively, denoted by  $b_{fs}$ ,  $t_{fs}$ ,  $h_{ws}$ , and  $t_{ws}$  and for the rings flange and web they are  $b_{fr}$ ,  $t_{fr}$ ,  $h_{wr}$ , and  $t_{wr}$ .  $d_s$  and  $d_r$  denote the distances between two stringers and rings, respectively, and the eccentricities  $e_s$  and  $e_r$  denote the distance from the middle surface of shell to the centroid of the stiffener cross-section (Figure 2).

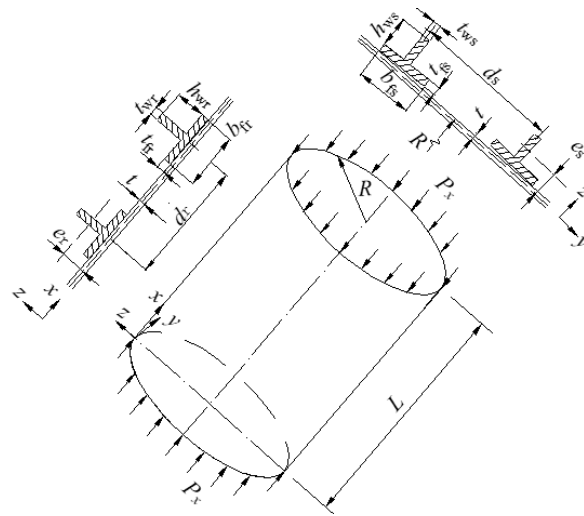


Figure 2. Configuration of an eccentrically stiffened cylindrical shell.

Based on Donnell's assumptions, the nonlinear geometric equations of stiffened cylinders with initial geometric imperfection are given as follows [39].

$$\begin{aligned} l\varepsilon_x &= u_{,x} + \frac{1}{2}(w_{,x})^2 + w_{,x}\bar{w}_{,x}, \quad \varepsilon_y = v_{,y} + \frac{w}{R} + \frac{1}{2}(w_{,y})^2 + w_{,y}\bar{w}_{,y}, \\ \gamma_{xy} &= u_{,y} + v_{,x} + w_{,x}w_{,y} + w_{,x}\bar{w}_{,y} + \bar{w}_{,x}w_{,y}, \\ \chi_x &= -w_{,xx}, \quad \chi_y = -w_{,yy}, \quad \chi_{xy} = -w_{,xy}. \end{aligned} \quad (6)$$

The strain energy of stiffened cylinders can be defined as shown [40]:

$$U = \frac{1}{2} \int_0^{2\pi R} \int_0^L (N_x \varepsilon_x + N_{xy} \gamma_{xy} + N_y \varepsilon_y + M_x \chi_x + 2M_{xy} \chi_{xy} + M_y \chi_y) dx dy \quad (7)$$

where  $L$  and  $R$  denote the cylindrical shell lengths in the axial and radial directions, respectively.

The work produced by axial forces of the structure can be expressed as shown [41]:

$$U_L = - \int_0^{2\pi R} \int_0^L P_x u_{,x} dx dy \quad (8)$$

Substituting Equations (7) and (8) into Equation (2) yields the following:

$$\begin{aligned} \Pi &= \frac{1}{2} \int_0^{2\pi R} \int_0^L \{ A_{11} [u_{,x} + \frac{1}{2}(w_{,x})^2 + w_{,x}\bar{w}_{,x}]^2 + A_{22} [v_{,y} + \frac{w}{R} + \frac{1}{2}(w_{,y})^2 + w_{,y}\bar{w}_{,y}]^2 \\ &+ 2A_{12} [u_{,x} + \frac{1}{2}(w_{,x})^2 + w_{,x}\bar{w}_{,x}] [v_{,y} + \frac{w}{R} + \frac{1}{2}(w_{,y})^2 + w_{,y}\bar{w}_{,y}] \\ &+ A_{66} (u_{,y} + v_{,x} + w_{,x}w_{,y} + w_{,x}\bar{w}_{,y} + \bar{w}_{,x}w_{,y})^2 - 2B_{11} w_{,xx} [u_{,x} + \frac{1}{2}(w_{,x})^2 + w_{,x}\bar{w}_{,x}] \\ &- 2B_{22} w_{,yy} [v_{,y} + \frac{w}{R} + \frac{1}{2}(w_{,y})^2 + w_{,y}\bar{w}_{,y}] + D_{11} w_{,xx} w_{,xx} + 2D_{12} w_{,xx} w_{,yy} \\ &+ D_{22} w_{,yy} w_{,yy} + 2D_{66} w_{,xy} w_{,xy} - 2P_x u_{,x} \} dx dy \end{aligned} \quad (9)$$

Prototype structural parameters can be expressed by the model structural parameters and scaling factors.

$$\begin{aligned} x_p &= C_x x_m, \quad y_p = C_y y_m, \quad u_p = C_u u_m, \quad v_p = C_v v_m, \quad w_p = C_w w_m, \\ \bar{w}_p &= C_{\bar{w}} \bar{w}_m, \quad (A_{ij})_p = C_{A_{ij}} (A_{ij})_m, \quad (B_{ij})_p = C_{B_{ij}} (B_{ij})_m, \\ (D_{ij})_p &= C_{D_{ij}} (D_{ij})_m, \quad R_p = C_R R_m, \quad (P_x)_p = C_{P_x} (P_x)_m. \end{aligned} \quad (10)$$

Assuming that the skins of two similitude structures conform to complete geometric similarity, i.e.,  $C_x = C_y = C_R = C_u = C_v = C_w = C_{\bar{w}}$ , the necessary conditions for the models

to predict accurately the prototype are obtained by applying the similitude transformation to Equation (9) as follows.

$$C_{A_{11}} = C_{A_{12}} = C_{A_{22}} = C_{A_{66}} = \frac{C_{B_{11}}}{C_R} = \frac{C_{B_{22}}}{C_R} = \frac{C_{D_{11}}}{C_R^2} = \frac{C_{D_{12}}}{C_R^2} = \frac{C_{D_{22}}}{C_R^2} = \frac{C_{D_{66}}}{C_R^2} = C_{P_x} \quad (11)$$

From Equation (11), the necessary similitude conditions between the model and its prototype can be obtained:

$$C_{A_{11}} = C_{A_{12}} = C_{A_{22}} = C_{A_{66}} \quad (12)$$

$$C_{B_{11}} = C_{B_{22}} \quad (13)$$

$$C_{D_{11}} = C_{D_{12}} = C_{D_{22}} = C_{D_{66}} \quad (14)$$

$$C_{A_{ij}} C_R^2 = C_{B_{ij}} C_R = C_{D_{ij}} \quad (15)$$

The similitude condition of the buckling mode shapes of the two systems can be defined as shown:

$$C_m = C_n = 1 \quad (16)$$

where  $m$  and  $n$  are the numbers of the half-waves of cylindrical shells in the longitudinal and circumferential directions, respectively.

Consider the stiffened cylinders subjected to in-panel, uniaxial compression load  $P_x$  (positive in compression). Assuming non-dimensional axial compression load  $K_{P_x} = P_x R^2 / (\pi^2 D_{11})$ , therefore,  $C_{P_x} = C_{K_{P_x}} C_{D_{11}} / C_R^2$ , the similitude invariant of post-buckling can be written as:

$$C_{P_x} C_R^2 / C_{\text{stiff}} = 1 \quad (17)$$

where  $C_{\text{stiff}}$  is  $C_{A_{ij}} C_R^2$  or  $C_{B_{ij}} C_R$  or  $C_{D_{ij}}$ .

The scaling law for post-buckling of stiffened cylinders under axial compression can be derived:

$$(P_x)_p = (P_x)_m \frac{C_{\text{stiff}}}{C_R^2} = (P_x)_m C_{\text{stiff}} \left( \frac{R_m}{R_p} \right)^2 \quad (18)$$

where  $P_x$  is the axial compression load in the x-direction.

### 3. Method for Post-Buckling Analysis of Stiffened Cylinders under Axial Compression

Thin-walled stiffened cylinders usually undergo buckling when the stress of the structure is notably low and does not reach the yield strength. Therefore, the influence of material nonlinearity cannot be considered in the post-buckling analysis of stiffened cylinders subjected to axial compression. The stiffened cylinder constructed of skin and ribs always incurs certain geometric imperfections in the process of manufacture and use. The post-buckling bearing capacity of the reinforced cylinder with geometrical imperfections is lower than that of the perfect structure. For accurate prediction of the post-buckling behavior of stiffened cylinders with geometric imperfections, the load-displacement curves must be tracked throughout the entire process.

The basic concept of the arc length (AR) method uses vector mechanics to describe the equilibrium paths of the structure. The development trend of the nonlinear process is controlled through an introduced constraint condition based on the original structural balancing equations. Currently, the AR method improved by Crisfield [42] is generally used in post-buckling analysis. The AR method can be applied to perform unstable and stable buckling analysis. The post-buckling stage of stiffened cylinders under axial compression is generally unstable buckling, and thus, the AR method is used to track the load-displacement path of structural buckling.

#### 4. Verification of Post-Buckling of Cylinders under Axial Compression

The reliability and accuracy of the finite element analysis in this paper is verified by comparing the results from the finite element analysis with those from the literature.

Figure 3 shows the results obtained from post-buckling analysis for eigenvalue modal imperfection (EMI) of three different amplitudes (imperfection factor  $\xi = 0.1, 0.5$ , and  $1.0$  for eigenmode  $m = 1, n = 10$ ). The relative errors of the buckling limit loads for the three imperfection amplitudes are presented in Table 1.

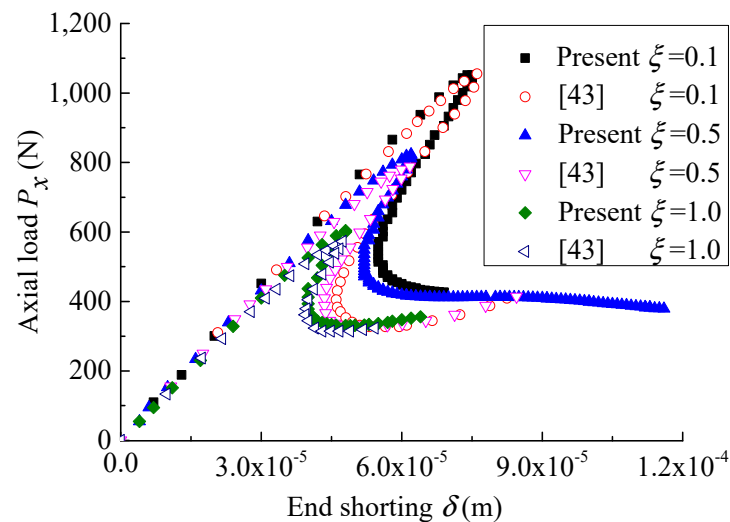


**Figure 3.** Comparison of present load-displacement results with those of the reference.

**Table 1.** Comparison of the buckling limit loads of the cylinder with different imperfection factors.

	$\xi = 0.1$	$\xi = 0.5$	$\xi = 1.0$
$P_{cl}$ Present (N)	1051.5	823.4	604.1
$P_{cl}$ [43] (N)	1045	784	557
error (%)	0.62%	5.02%	8.46%

The material and geometric parameters of the longitudinal stiffened cylinders XS-1 and AS-2 [44,45] are shown in Table 2. The boundary conditions at both ends of the structure are classical simply supported (SS3) or fixed support (C3), and the expressions of the boundary conditions are given by Equations (19) and (20), respectively. In the finite element analysis, axial constraints are added at two symmetrical node positions along the  $\frac{1}{2}$  height of the stiffened cylinder to prevent rigid body displacement of the structure. The skin is only restricted at the end of the stiffened cylinder, and the axial compression load is applied to the end faces of the shell and the reinforced section (i.e., the most unfavorable constraints and loads are used).

**Table 2.** Geometric and material properties of stringer-stiffened cylinders.

	$E$ (Gpa)	$\mu$	$R$ (mm)	$L$ (mm)	$t$ (mm)	$h_s$ (mm)	$t_s$ (mm)	$N_s$
XS-1	68.95	0.3	101.6	101.6	0.196596	0.475488	1.67894	80
AS-2	68.95	0.3	101.6	139.7	0.196596	0.475488	1.67894	80

The SS3 boundary conditions are given as follows:

$$w = M_x = v = N_x \quad (19)$$

The C3 boundary conditions are given as follows:

$$w = w_{,x} = v = N_x \tag{20}$$

Based on the finite element model of longitudinal stiffened cylinders, post-buckling analysis under axial compression is performed by introducing an ideal disturbance displacement imperfection (IDDI). The expression of two-modal idealized imperfection can be as follows [44,45]:

$$\bar{w} = -0.01 \cos\left(\frac{2\pi x}{L}\right) + 0.50 \sin\left(\frac{\pi x}{L}\right) \cos\left(\frac{ny}{R}\right) \tag{21}$$

Comparisons of the results for axial compression buckling of the stringer-stiffened cylinder XS-1 are presented in Table 3. If the boundary conditions of XS-1 are SS3 and C3, the error between the buckling limit load of the finite element and the result of the literature [44] is  $-4.45\%$  and  $-17.48\%$ , respectively, and the buckling mode shape is (1, 11). The reasons for the discrepancy in the buckling ultimate load are listed as follows: ① the smeared stiffener theory is adopted in the literature, ② the effects of load eccentricity are not considered in the literature, and ③ rotation constraints and in-plane boundaries have a great influence on the external longitudinal stiffened cylinders. If the boundary condition of XS-1 is SS3, the post-buckling limit load of axial compression compared with the linear buckling load of the perfect structure is reduced by 40.6%, and the discrepancy is  $-4.19\%$  compared with the result of the literature [44]. If the boundary condition is C3, the post-buckling limit load of axial compression is reduced by 40.7%, and the error is  $-5.87\%$  compared with the result of the literature [44]. The results for axial compression buckling of the stringer-stiffened cylinder AS-2 are presented in Table 4.

**Table 3.** Comparisons of buckling results (N/m) for the stringer-stiffened cylinder XS-1 under axial load.

	SS3			C3		
	[44]	Present	Error (%)	[44]	Present	Error (%)
$P_{cr}$	24,780 (1,11)	24,694 (1,11)	-0.35	28,280 (1,12)	24,964.7 (1,11)	-11.72
$P_{lim}$	15,347.5 (1,11)	14,665.3 (1,11)	-4.45	17,937.5 (1,11)	14,802.3 (1,11)	-17.48
$\rho_s$	0.62	0.594	-4.19	0.63	0.593	-5.87

Note:  $P_{cr}$ —linear buckling load of perfect structure,  $P_{lim}$ —axial post-buckling ultimate load of structures with initial geometric imperfection;  $(m, n)$ — $m$  axial half-wavenumber,  $n$ —circumferential wavenumber;  $\rho_s = P_{lim}/P_{cr}$ .

**Table 4.** Comparison of the axial buckling results (N/m) for the stringer-stiffened cylindrical shell AS-2.

	SS3			C3		
	[45]	Present	Error (%)	[45]	Present	Error (%)
$P_{cr}$	22,980 (1,10)	22,824 (1,10)	-0.68	25,687 (1,10)	22,988.5 (1,10)	-10.5
$P_{lim}$	13,858 (1,10)	15,054 (1,10)	8.63	15,700 (1,10)	15,146.4 (1,10)	-3.53
$\rho_s$	0.60	0.660	10.0	0.61	0.659	8.03

Note:  $P_{cr}$ —linear buckling load of perfect structure,  $P_{lim}$ —axial post-buckling ultimate load of structures with initial geometric imperfection;  $(m, n)$ — $m$  axial half-wavenumber,  $n$ —circumferential wavenumber;  $\rho_s = P_{lim}/P_{cr}$ .

Post-buckling of the cylinder with dimple imperfections (DI) under axial compression in the literature [46] is taken as the example for verification. The geometric and material parameters of the cylinder with DI are  $L = 0.51$  m,  $R = 0.25$  m,  $t = 0.0005$  m,  $E = 72$  GPa, and  $\mu = 0.31$  [46]. The axial displacement constraint for the upper boundary of the structure only is released, while the lower boundary of the structure is a fixed support.

The applied dimple imperfection function can be expressed as [46]:

$$\delta_a(s) = \delta_0 e^{-\pi s/\lambda} \cos \frac{\pi s}{\lambda} \quad (22)$$

$$s = \sqrt{(R\theta - R\theta_0)^2 + (z - z_0)^2} \quad (23)$$

where  $\delta_0$  is the imperfection amplitude,  $\lambda$  is the imperfection diameter,  $\theta_0$  and  $z_0$  denote the circumferential and longitudinal coordinate values of the imperfection center, and  $s$  denotes the distance from the imperfection center to the finite element grid node within the imperfection range. The dimple imperfection is applied to the perfect cylinder model by using static analysis and updating the node coordinates.

The AR method with force loading is used for validation. Table 5 shows the errors between the results obtained by the AR method and the literature results when  $\delta_0 = 0.5 t$  and  $\lambda$  equals 0.05 m, 0.06 m and 0.07 m, respectively [25]. It can be found from Table 5 that the AR method APDL program for post-buckling of cylinders under axial compression is reliable and accurate.

**Table 5.** Comparison of post-buckling ultimate loads of cylinders with DI under axial compression.

$\delta_0/m$	$\lambda/m$	Literature [46]/kN	AR Method/kN	Error/%
0.5 $t$	0.05	42.18	43.90	4.08%
	0.06	42.29	44.04	4.14%
	0.07	42.38	43.96	3.73%

## 5. Post-Buckling Similarity Simulation of Axial Compression Based on Three Different Geometrical Imperfections

Finite element models were established in ANSYS, and the SHELL181 element was used to divide the stiffened cylinders. According to the suggestion of Meyer–Piening [47], the size of the shell element should be no greater than  $0.5\sqrt{Rt}$ . For the stiffened cylinders, the skins between two adjacent stiffeners should be divided into at least 8 equal portions, and the webs of the stiffeners are divided into 3 to 5 equal portions along the height direction. The flanges of stiffeners should be divided into 4 equal portions. Post-buckling analysis of stiffened cylinders subjected to axial compression is solved by the AR method.

The effective shell wall thicknesses of the densely stiffened orthotropic cylinders  $t_{\text{eff}}$  is defined as [37]:

$$t_{\text{eff}} = \sqrt[4]{\frac{144D_{11}D_{22}}{A_{11}A_{22}}} \quad (24)$$

The effects of the radius to effective thickness ratios, boundary conditions, and stiffened cross-sections for similitude simulation are investigated. The material parameters of scale models are the data of Table 6 [27].

**Table 6.** Material parameters of scaled models.

Material	$E/GPa$	$\mu$
Aluminum	68.75	0.30
Brass	106	0.34
Copper	124	0.33
PVC	3.79	0.40

The scaling law of axial compression post-buckling load in Equation (18) can be simplified as follows:

$$C_{P_x} = kk_1 \quad (25)$$

### 5.1. Post-Buckling Similarity Simulation of Axial Compression Based on First-Order EMI

The geometric and material parameters of the longitudinal ring rectangular stiffened cylinder (LRRSC) and the longitudinal ring T-type stiffened cylinder (LRTSC) are listed in Table 7. The ends of the skin of the stiffened cylinders are constrained, and the geometric scale factors are equal to 10.

**Table 7.** Geometric and material properties of longitudinal ring stiffened cylinders.

LRRSC	<b>E (GPa)</b> 72.3975	$\mu$ 0.3	<b>R</b> 2425.7	<b>L</b> —	<b>t</b> 12.7	$h_r$ 76.708	$h_s$ 76.708	$t_r$ 24.384	$t_s$ 24.384	$d_r$ 254	$d_s$ 254	<b>R/t<sub>eff</sub></b> 23.7618
LRTSC	<b>E (GPa)</b> 206	$\mu$ 0.3	<b>R</b> 3230	<b>L</b> 12,600	<b>t</b> 18	$b_{fr}, b_{fs}$ 175	$h_{wr}, h_{ws}$ 75	$t_{fr}, t_{fs}$ 18	$t_{wr}, t_{ws}$ 15	$N_r$ 24	$N_s$ 72	<b>R/t<sub>eff</sub></b> 40.004

Note: The unit of length is millimeter—based on different aspect ratios ( $L/R = 1.26, 2.51, \text{ and } 3.77$ ).

In the finite element analysis, based on the first-order eigenvalue buckling mode and introduction of the imperfection factor  $\zeta$ , imperfect structure models were obtained by introducing imperfections into the perfect structural models and updating the node coordinates.

For stiffened cylinders with different aspect ratios ( $L/R = 1.26, 2.51, \text{ and } 3.77$ ), boundary conditions (SS3 and C3) and stiffened cross-sections (rectangular and T-type), similitude simulations for axial compression post-buckling with four imperfection factors (0.05, 0.1, 0.3, and 0.5) were performed based on the first-order EMI.

The partial similarities for axial compression post-buckling of LRRSC with the C3 boundary condition are similar to those of structures with the SS3 boundary condition. Only partial similarities are given for axial compression post-buckling of structures with  $L/R = 2.51$  and the SS3 boundary condition.

If the material of the model is AL, Figure 4 shows the results of partial similarity and the equilibrium paths of the models for axial compression post-buckling of rectangular stiffened cylinders with  $L/R = 2.51$ , the SS3 boundary condition and four different geometric imperfections ( $\zeta = 0.05, 0.1, 0.3, \text{ and } 0.5$ ). As shown in Figure 4a–d, the equilibrium paths of the models can primarily predict the results of its prototype using the scaling law Equation (25) and the deformation scaling factor. As observed from Figure 4e, the slope of the linear phase curve gradually decreases as the imperfection factor increases in the initial stage of loading. When  $\zeta = 0.05$  and 0.1, the type of structural buckling belongs to limit-point instability. When the imperfect factor is small, the limit point of the equilibrium path extends far to a tip, and the buckling limit load gradually decreases as the imperfection factor increases. When  $\zeta > 0.1$ , the axial compression buckling bearing capacity of structures shows the characteristic of monotonously stable increase. For  $\zeta = 0.5$ , the deviation between the predicted displacement and the finite element result is large at the end of the post-buckling equilibrium path, because large deformation is produced by a slight change of the load at the end of the equilibrium path. The buckling mode shape (3,5) of the model with  $\zeta = 0.05$  at the limit point of the equilibrium path is shown in Figure 5 and is the same as the shape at the corresponding point of the prototypical equilibrium path. When  $\zeta = 0.05$  and 0.1, the discrepancies between the predicted axial compression limit loads  $P_{x\text{lim}_p\text{pre}}$  and the axial compression limit loads of the prototype  $P_{x\text{lim}_p}$  are  $-0.92\%$  and  $-0.83\%$ , respectively.

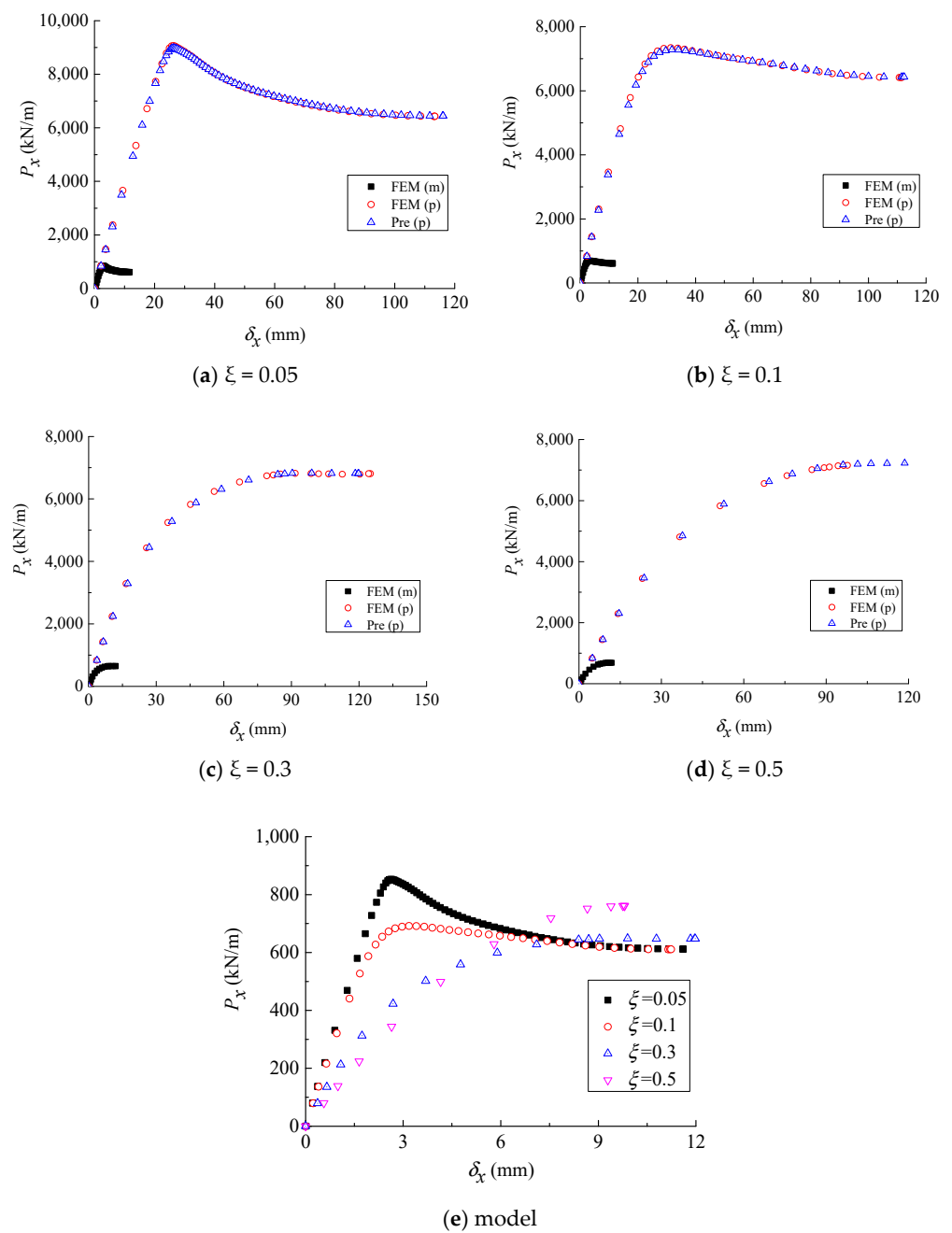


**Figure 4.** Comparison of the predicted and original load vs. end-shortening curves of the stiffened cylindrical shells with  $L/R = 2.51$  and the SS3 boundary condition when the material of the model is AL.

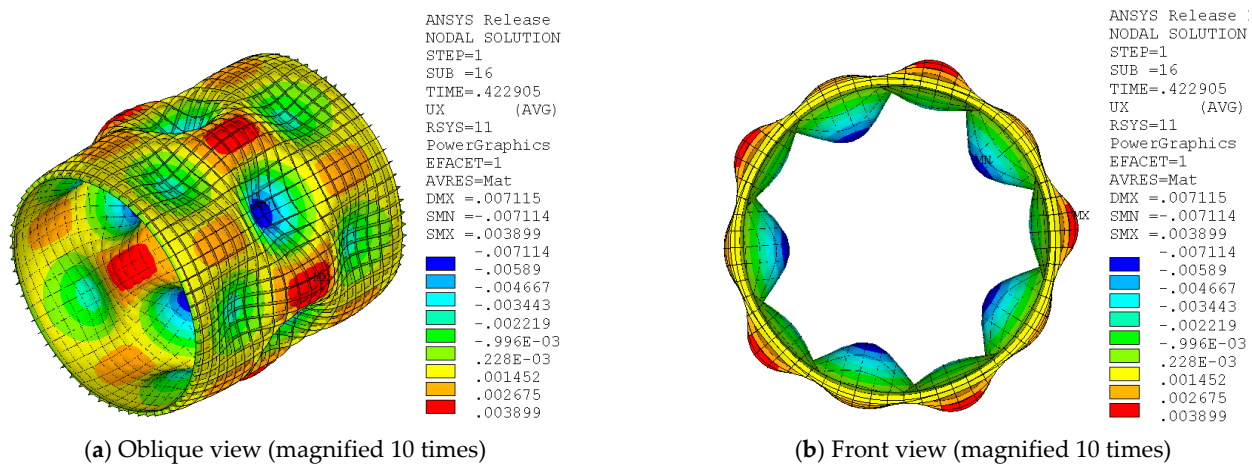


**Figure 5.** Radial displacement contour map at the critical point of the post-buckling path for the model of the stiffened cylinders with  $L/R = 2.51$  and the SS3 boundary condition when the material is AL and  $\xi = 0.05$ .

When the material of the model is brass, Figure 6 demonstrates the results of partial similarity and the equilibrium paths of the models for axial compression post-buckling of rectangular stiffened cylinders with  $L/R = 2.51$ , the SS3 boundary condition, and four different geometric imperfections. As demonstrated by Figure 6a–d, the equilibrium paths of the models can satisfactorily predict the results of its prototype using the scaling law Equation (18) and the deformation scaling factor. It can be noted from Figure 6e that the change rule for the equilibrium paths of the model is similar to that in Figure 4e. The buckling mode shape (3,5) of the model with  $\xi = 0.05$  at the limit point of the equilibrium path is given in Figure 7, which is the same as the shape at the corresponding point of the prototypical equilibrium path. When  $\xi = 0.05$  and 0.1, the discrepancies between  $P_{x\text{lim}_p\text{-pre}}$  and  $P_{x\text{lim}_p}$  are  $-4.44\%$  and  $-3.71\%$ , respectively.

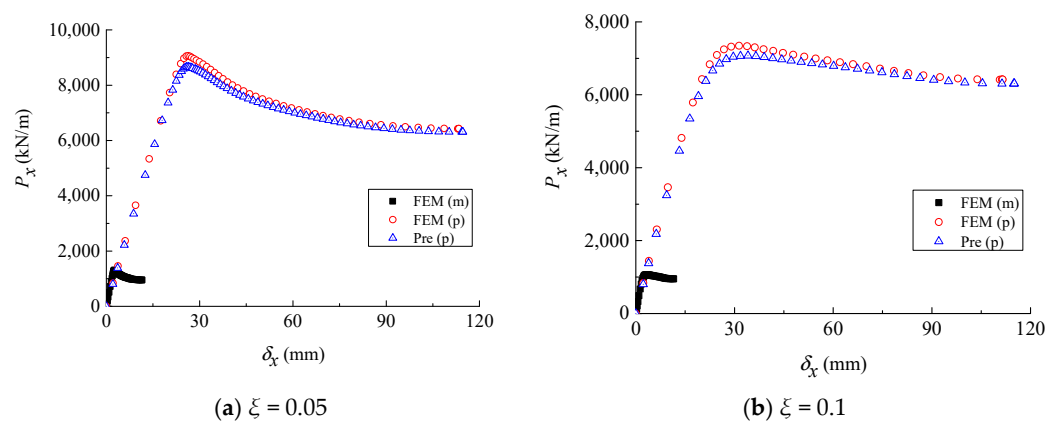


**Figure 6.** Cont.

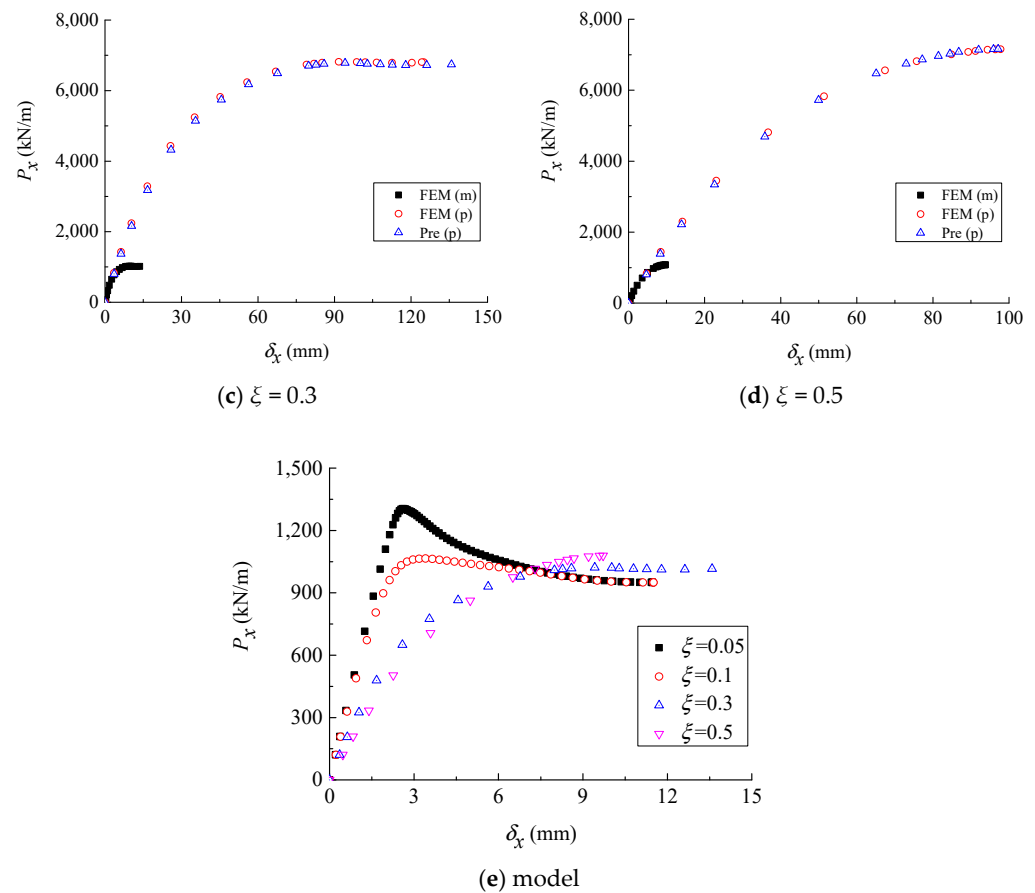


**Figure 6.** Comparison of the predicted and original load vs. end-shortening curves of the stiffened cylinders with  $L/R = 2.51$  and the SS3 boundary condition when the model material is brass.

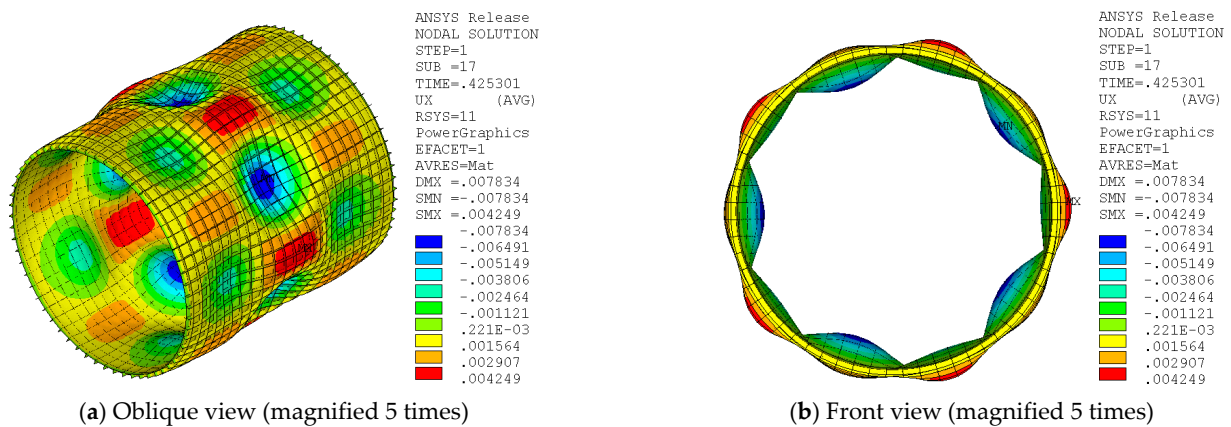


**Figure 7.** Radial displacement contour map at the critical point of the post-buckling path for the model of the stiffened cylinders with  $L/R = 2.51$  and the SS3 boundary condition when the material is brass and  $\xi = 0.05$ .

When the material of the model is PVC, Figure 8 shows the results of partial similarity and the equilibrium paths of the models for axial compression post-buckling of rectangular stiffened cylinders with  $L/R = 2.51$ , the SS3 boundary condition, and four different geometric imperfections. As shown in Figure 8a–d, the equilibrium paths of the models can reasonably predict the results of its prototype using the scaling law Equation (18) and the deformation scaling factor. It can be observed from Figure 8e that the change rule of the model equilibrium paths is similar to those of Figures 4e and 6e. The buckling mode

shape (3,5) of the model with  $\zeta = 0.05$  at the limit point of the equilibrium path is shown in Figure 9, which is the same as the shape at the corresponding point of the prototypical equilibrium path. When  $\zeta = 0.05$  and 0.1, the discrepancies between  $P_{x\text{lim\_p\_pre}}$  and  $P_{x\text{lim\_p}}$  are  $-8.65\%$  and  $-6.76\%$ , respectively.

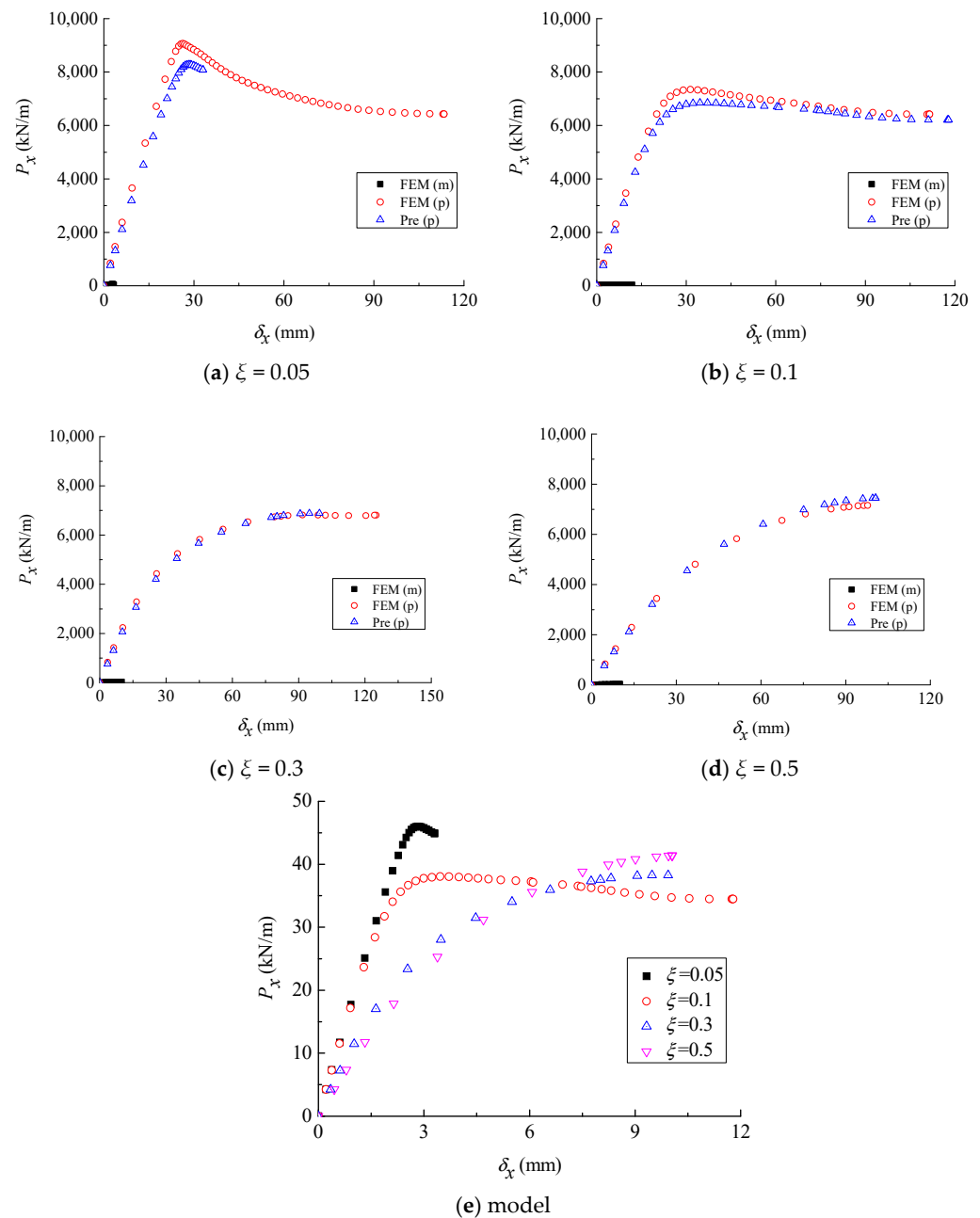


**Figure 8.** Comparison of the predicted and original load vs. end-shortening curves of the stiffened cylinders with  $L/R = 2.51$  and the SS3 boundary condition when the model material is PVC.

When the material of the model is AL, Figure 10 shows the results of partial similarity and the equilibrium paths of the models for axial compression post-buckling of T-type stiffened cylinders with the SS3 boundary condition and four different geometric imperfections ( $\zeta = 0.05, 0.1, 0.3,$  and  $0.5$ ). As shown in Figure 10a–d, the equilibrium paths of the models can predict the results of its prototype using the scaling law Equation (25) and the deformation scaling factor. At the limit points of the equilibrium paths, the buckling mode shapes of the models are both (1,3), and only the case of  $\zeta = 0.05$  is given, as shown in Figure 11.

Figure 10e depicts the equilibrium paths of the models. At the initial stage of loading, the slope of the linear phase curve gradually decreases as the imperfect factor increases. When  $\zeta = 0.05$  and  $0.1$ , the type of structural buckling is snap-through buckling. A longer post-buckling path of partial models cannot be given because the capability for post-buckling analysis in ANSYS finite element software is not strong. When the imperfection factor is small, the limit loads of the structures under axial compression gradually decrease with the increasing imperfection factor. When  $\zeta > 0.1$ , no extreme point appears in the equilibrium paths, and the load-carrying capacity of the structures under axial compression gradually decreases as the imperfection factor increases in the post-buckling stage. When  $\zeta = 0.05$ , the discrepancy between  $P_{x\text{lim}_p\text{pre}}$  and  $P_{x\text{lim}_p}$  is  $-8.21\%$ . When  $\zeta = 0.1$ , the discrepancy between  $P_{x\text{lim}_p\text{pre}}$  and  $P_{x\text{lim}_p}$  is  $-13.03\%$ , and the discrepancy is  $-5.93\%$  for the lower critical load.

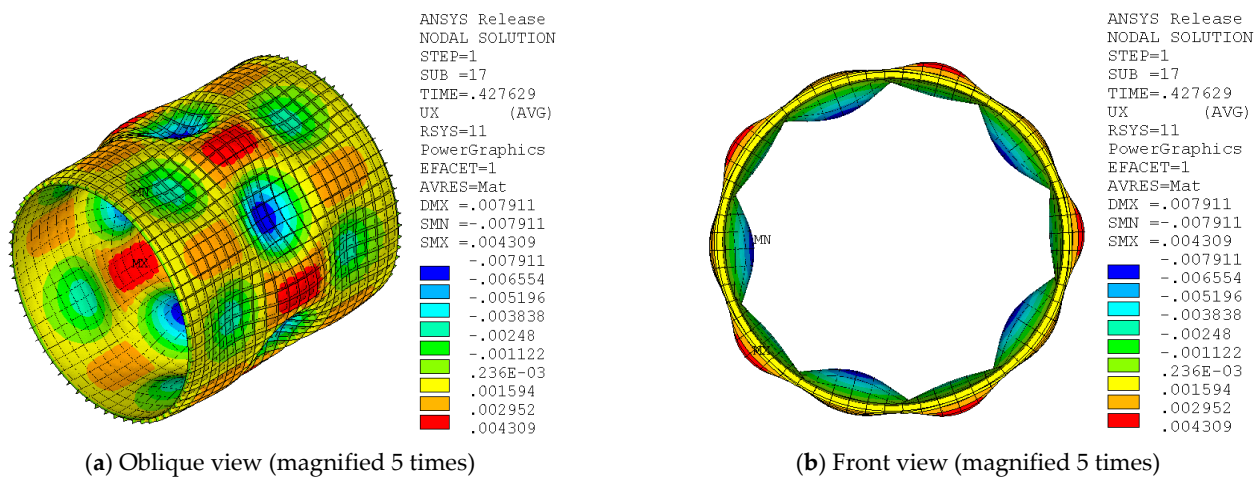


**Figure 9.** Radial displacement contour map at the critical point of the post-buckling path for the model of the stiffened cylinders with  $L/R = 2.51$  and the SS3 boundary condition when the material is PVC and  $\zeta = 0.05$ .

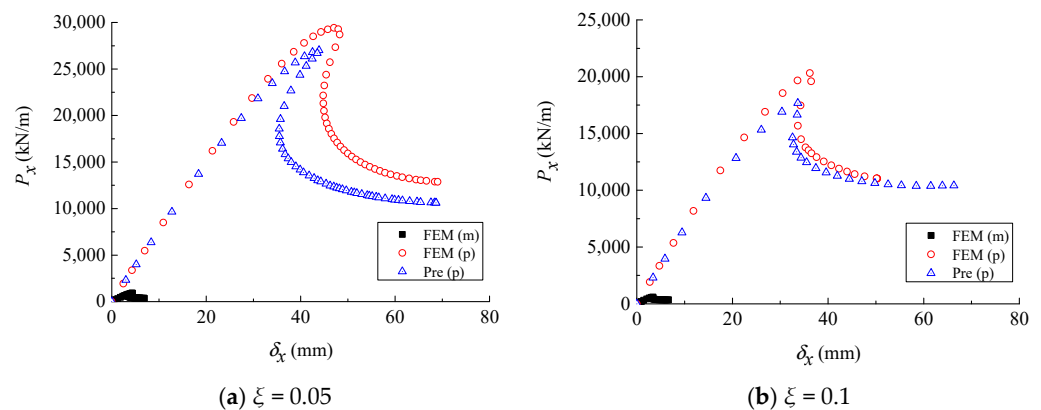


**Figure 10.** Cont.

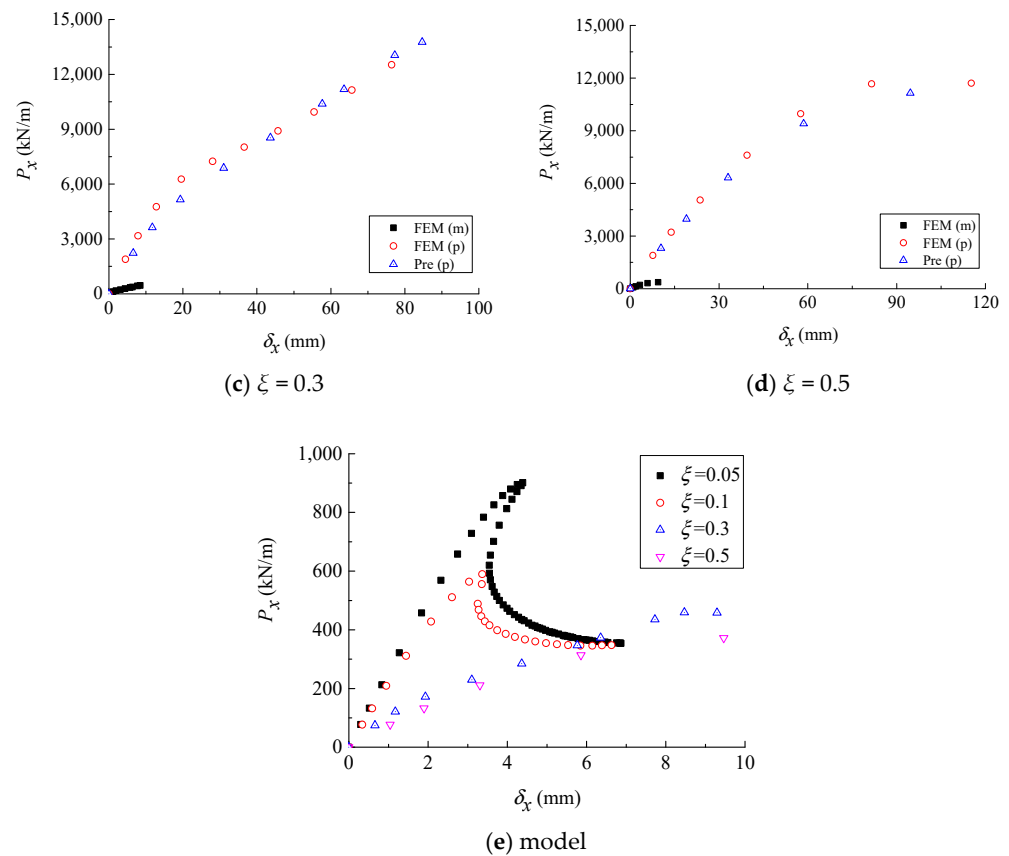


Figure 10. Comparison of the predicted and original load vs. end-shortening curves of the T-type stiffened cylinders with the SS3 boundary condition when the model material is AL.

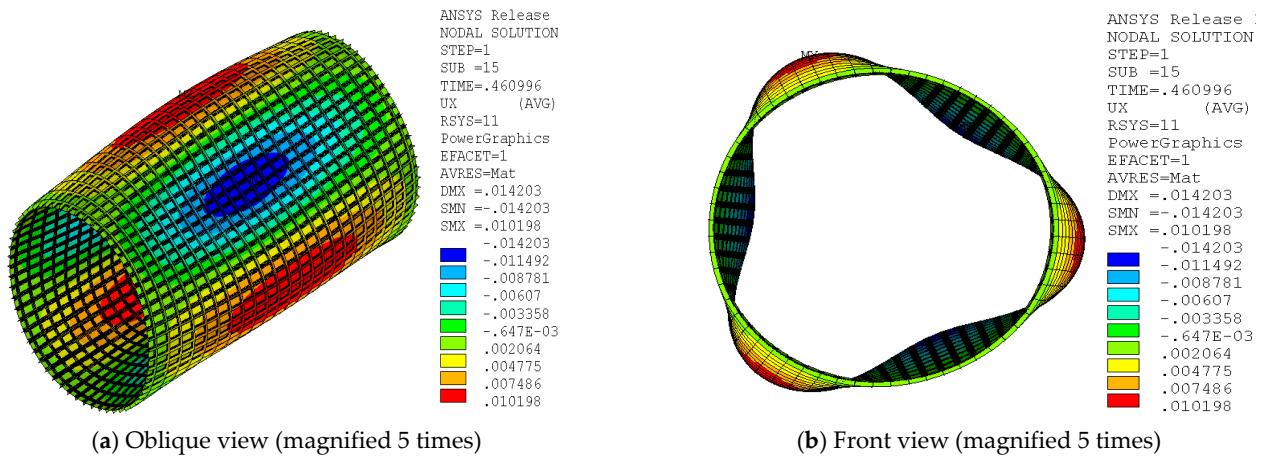
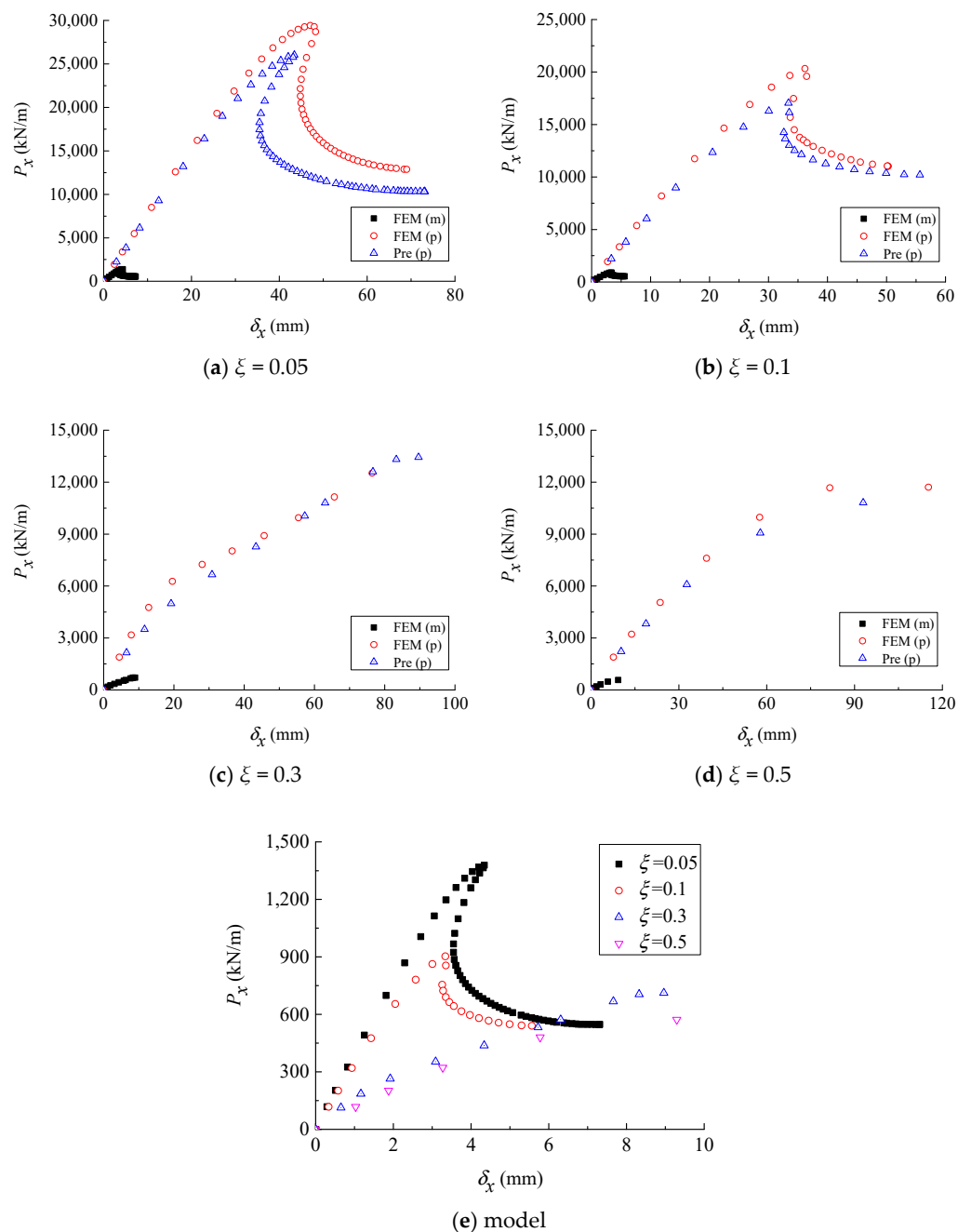


Figure 11. Radial displacement contour map at the upper critical point of the post-buckling path for the model of the T-type stiffened cylinders with the SS3 boundary condition when the material is AL and  $\zeta = 0.05$ .

When the material of the model is brass, Figure 12 presents the results of partial similarity and the equilibrium paths of the models for axial compression post-buckling of T-type stiffened cylinders with the SS3 boundary condition and four different geometric imperfections. As shown in Figure 12a–d, the equilibrium paths of the models can predict the results of its prototype using the scaling law Equation (18) and the deformation scaling factor. It can be noted from Figure 12e that the change rule of the equilibrium paths of the models is similar to that of Figure 10e. The buckling mode shapes of the models are (1,3) at the limit point of the equilibrium path, and only the case of  $\zeta = 0.05$  is given, as shown

in Figure 13. When  $\xi = 0.05$  and  $0.1$ , the discrepancies between  $P_{x\text{lim\_p\_pre}}$  and  $P_{x\text{lim\_p}}$  are  $-11.54\%$  and  $-16.1\%$ , respectively.



**Figure 12.** Comparison of the predicted and original load vs. end-shortening curves of the T-type stiffened cylinders with the SS3 boundary condition when the model material is brass.

When the material of the model is PVC, Figure 14 shows the results of partial similarity and the equilibrium paths of the models for axial compression post-buckling of T-type stiffened cylinders with the SS3 boundary condition and four different geometric imperfections. As shown in Figure 14a–d, the equilibrium paths of the models can predict the results of its prototype using the scaling law Equation (18) and the deformation scaling factor. As observed from Figure 14e, the change rule of equilibrium paths of the models is similar to those of Figures 10e and 12e. The buckling mode shapes of the models are (1,3) at the limit point of the equilibrium path, and only the case of  $\xi = 0.05$  is given, as shown

in Figure 15. When  $\zeta = 0.05$  and  $0.1$ , the discrepancies between  $P_{x\text{lim}_p\text{pre}}$  and  $P_{x\text{lim}_p}$  are  $-14.77\%$  and  $-19.36\%$ , respectively.

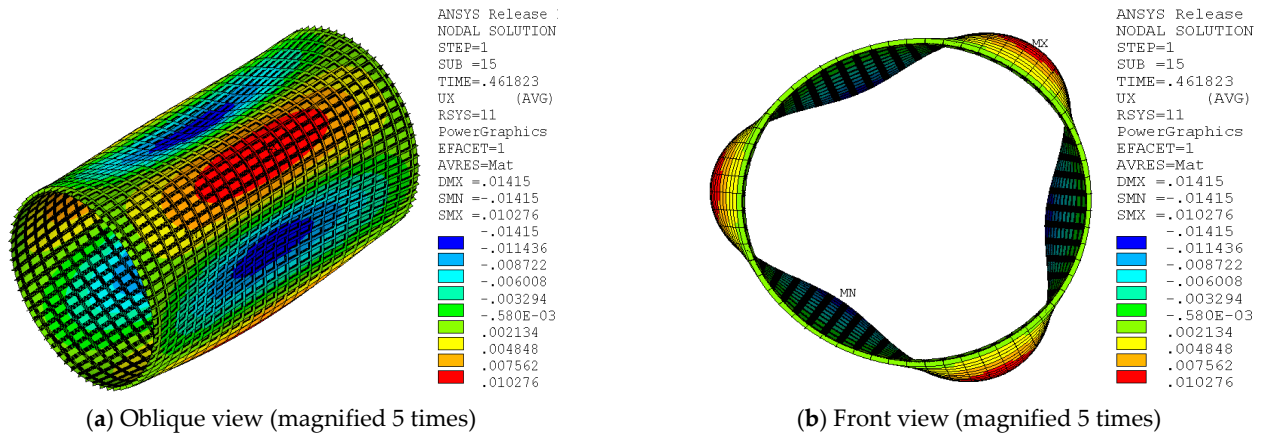


**Figure 13.** Radial displacement contour map at the upper critical point of the post-buckling path for the model of the T-type stiffened cylinders with the SS3 boundary when the material is brass and  $\zeta = 0.05$ .

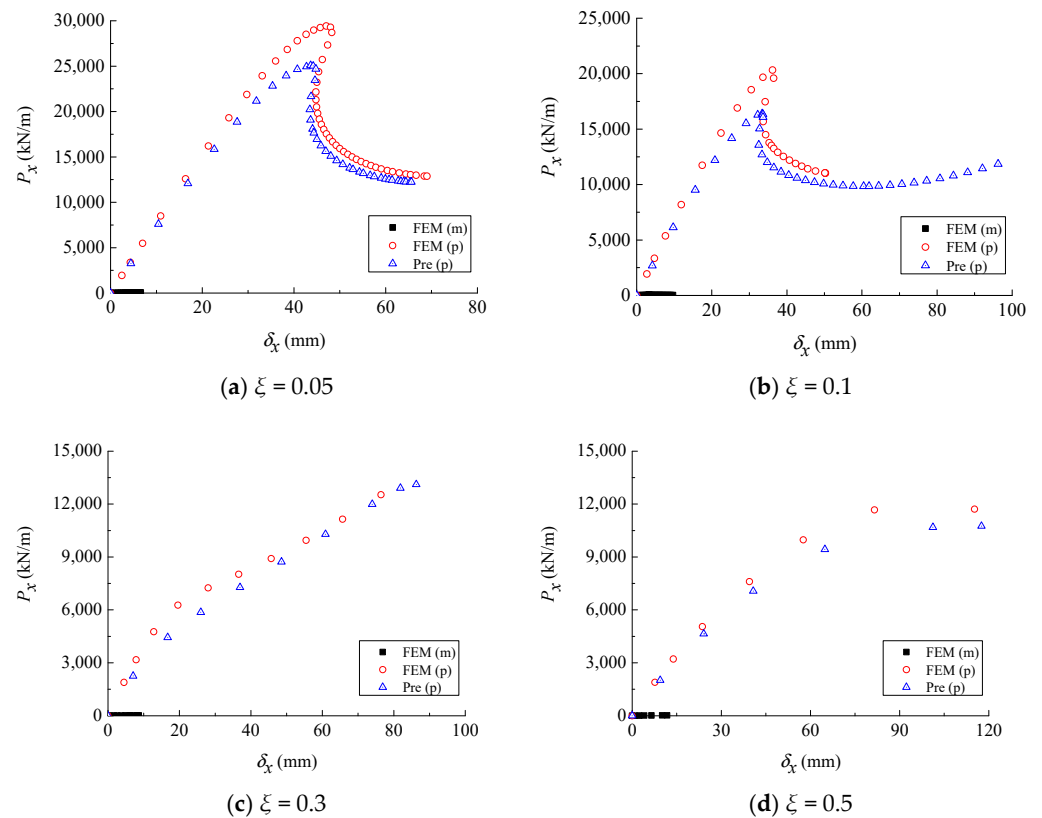


**Figure 14.** Cont.

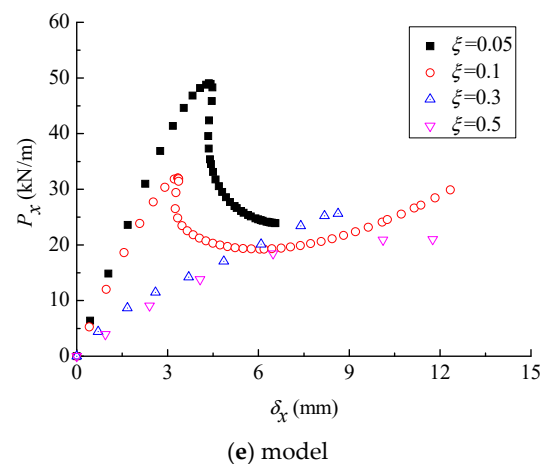


**Figure 14.** Comparison of the predicted and original load vs. end-shortening curves of the T-type stiffened cylinders with the SS3 boundary when the model material is PVC.

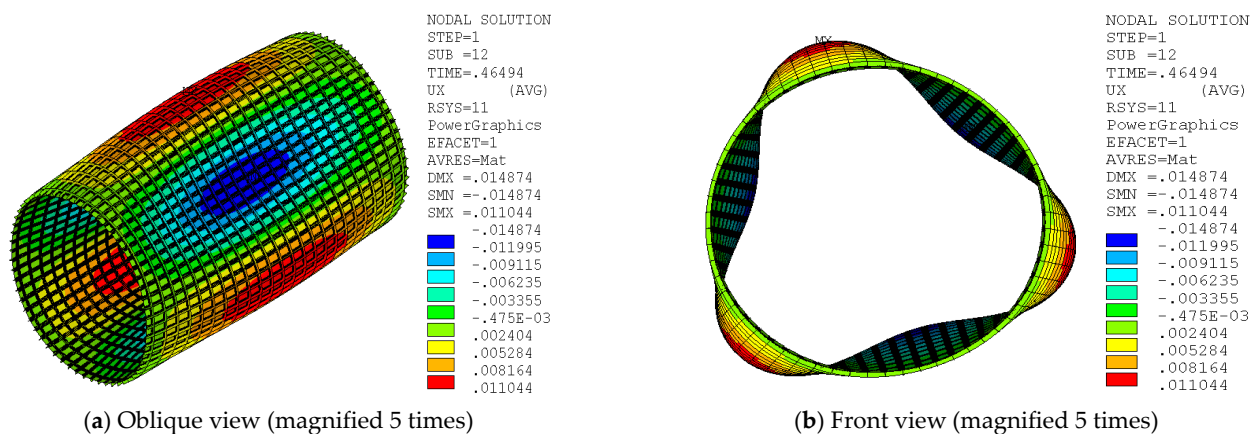


**Figure 15.** Radial displacement contour map at the upper critical point of the post-buckling path for the model of the T-type stiffened cylinder with the SS3 boundary condition when the material is PVC and  $\xi = 0.05$ .

The cases of post-buckling of longitudinal ring T-type stiffened cylinders with the C3 boundary condition are similar to those of the SS3 boundary condition, and the corresponding results are not given.

### 5.2. Post-Buckling Similarity Simulation of Axial Compression Based on IDDI

The parameters of the longitudinal rectangular stiffened cylinder (LRSC) are listed as follows:  $R = 1.016$  m,  $L = 1.397$  m,  $t = 1.96596 \times 10^{-3}$  m,  $h_s = 4.75488 \times 10^{-3}$  m,  $t_s = 16.7894 \times 10^{-3}$  m,  $N_s = 80$ ,  $E = 68.95$  GPa,  $\mu = 0.3$ ,  $L/R = 1.375$ , and  $R/t_{\text{eff}} = 268.9545$ . The boundary condition is SS3, and geometric scale factors are 10. For the geometric imperfection of a given function form, the node coordinates of the finite element model are updated based on static analysis, and the imperfections are introduced into the perfect finite element model. The similarity simulation for post-buckling of LRSC under axial compression was analyzed by ANSYS and MATLAB software based on the IDDI.

Using the ideal disturbance symmetric displacement imperfection given by Simites [48], post-buckling similarity simulation of imperfect structures with different imperfection amplitudes under axial compression was performed, and the correctness and universality of the scaling laws for the axial compression post-buckling proposed in this paper are further verified.

The functional expression of ideal perturbation symmetric displacement imperfection is written as shown [48]:

$$\frac{\bar{w}}{t} = \zeta \sin\left(\frac{\pi x}{L}\right) \cos\left(\frac{ny}{R}\right) \quad (26)$$

where  $\zeta = \bar{w}_{\max}/t$  is the imperfection amplitude factor. The four cases of imperfection are  $\zeta = 0.1, 0.3, 0.5,$  and  $1$ , respectively.

When the material of the model is brass, Figure 16 shows the results of the partial similarity for axial compression post-buckling of LRSC with the SS3 boundary condition and four different geometric imperfections. As shown in Figure 16a–d, the equilibrium paths of the models can well predict the results of its prototype using the scaling law Equation (18) and the deformation scaling factor. For the stiffness scaling factor  $C_{\text{stiff}} = (C_{D_{11}} + C_{D_{12}} + C_{D_{22}} + C_{D_{66}})/4$  in Equation (18), its specific value is 626.473. Figure 17 shows the buckling mode shapes at the upper and lower critical points of the equilibrium path of the model when  $\zeta = 0.1$ . When  $\zeta = 0.1, 0.3, 0.5,$  and  $1$ , the discrepancies between the predicted upper and lower critical loads and the corresponding results of the prototypes are  $-3.09\%$  and  $-2.43\%$ ,  $-2.90\%$  and  $-2.45\%$ ,  $-2.80\%$  and  $-2.46\%$ ,  $-2.70\%$  and  $-2.50\%$ , respectively. The first upper critical loads are considered as  $P_{x\text{lim}}$ .

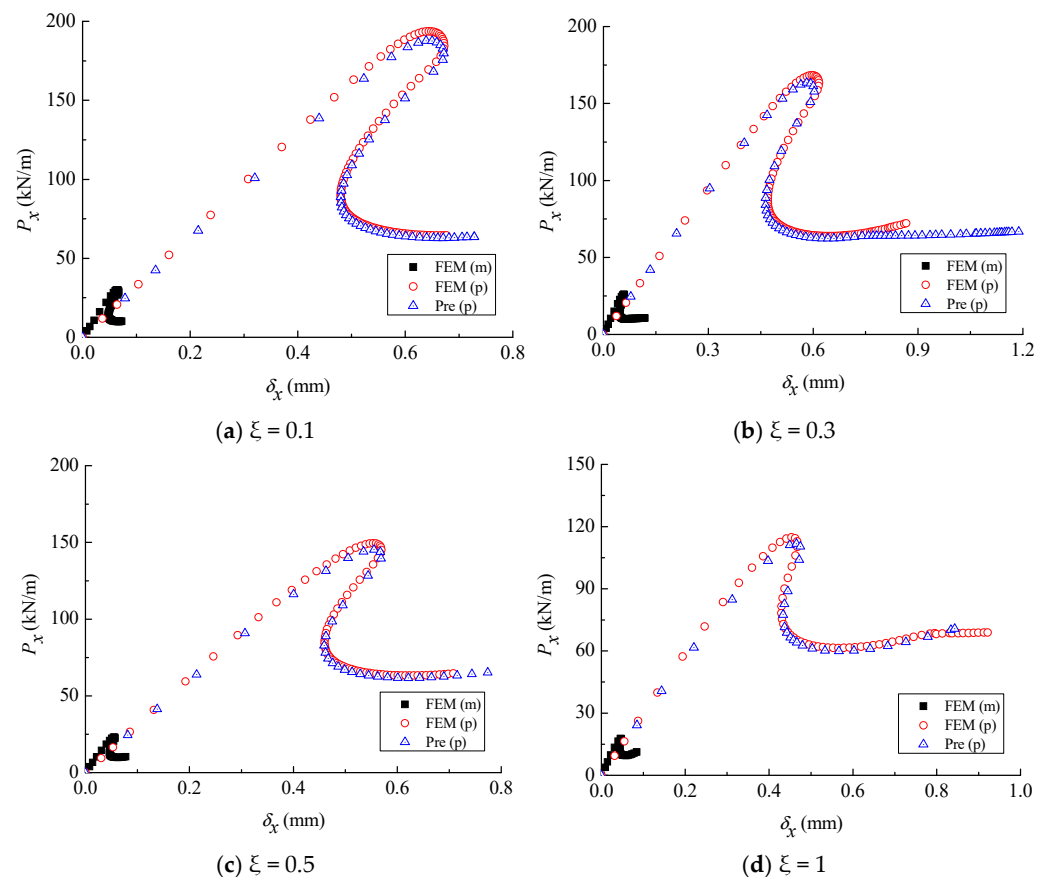


**Figure 16.** Comparison of the predicted and original load vs. end-shortening curves of the stringer-stiffened cylinders with the SS3 boundary condition when the model material is brass.

When the material of the model is PVC, Figure 18 presents the results of partial similarity for axial compression post-buckling of LRSC with the SS3 boundary condition and four different geometric imperfections. As shown by Figure 18a–d, the equilibrium paths of the models can well predict the results of its prototype using the scaling law Equation (18) and the deformation scaling factor. The stiffness scaling factor  $C_{\text{stiff}} = (C_{D_{11}} + C_{D_{12}} + C_{D_{22}} + C_{D_{66}})/4$  in Equation (18) has a specific value of 16,693.207. Figure 19 demonstrates the buckling mode shapes at the upper and lower critical points of

the equilibrium path of the model when  $\xi = 0.1$ . When  $\xi = 0.1, 0.3, 0.5$ , and 1, the discrepancies between the predicted upper and lower critical loads and the corresponding results of the prototypes are  $-6.37\%$  and  $-4.61\%$ ,  $-5.92\%$  and  $-4.63\%$ ,  $-5.74\%$  and  $-4.66\%$ ,  $-5.42\%$  and  $-4.74\%$ , respectively.

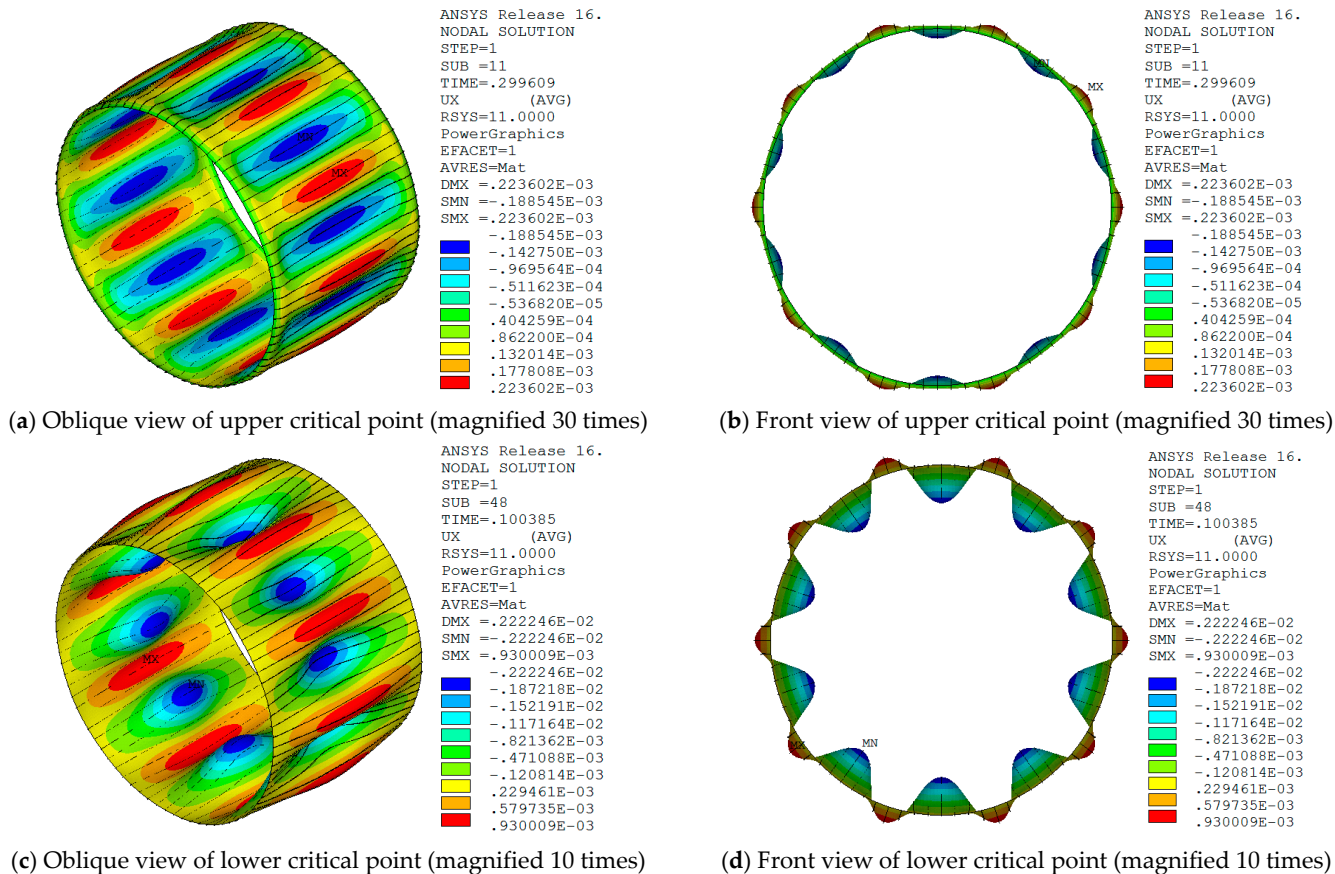


Figure 17. Radial displacement contour map at the critical points of the post-buckling path for the model with the SS3 boundary condition when the material of the model is brass and  $\xi = 0.1$ .

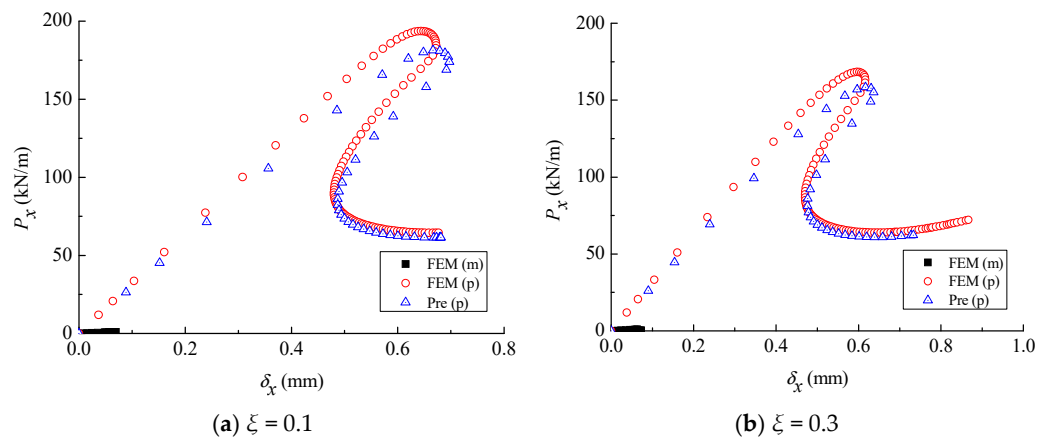


Figure 18. Cont.

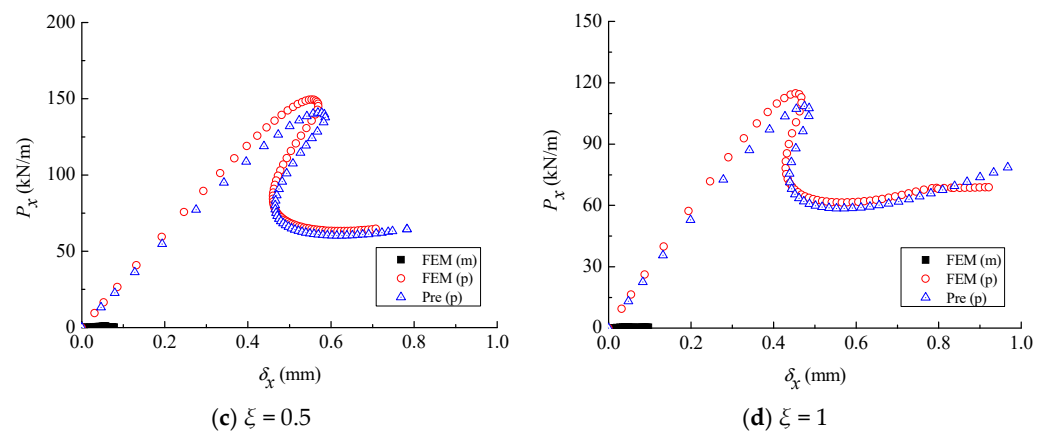


Figure 18. Comparison of the predicted and original load vs. end-shortening curves of the stringer-stiffened cylinders with the SS3 boundary condition when the model material is PVC.

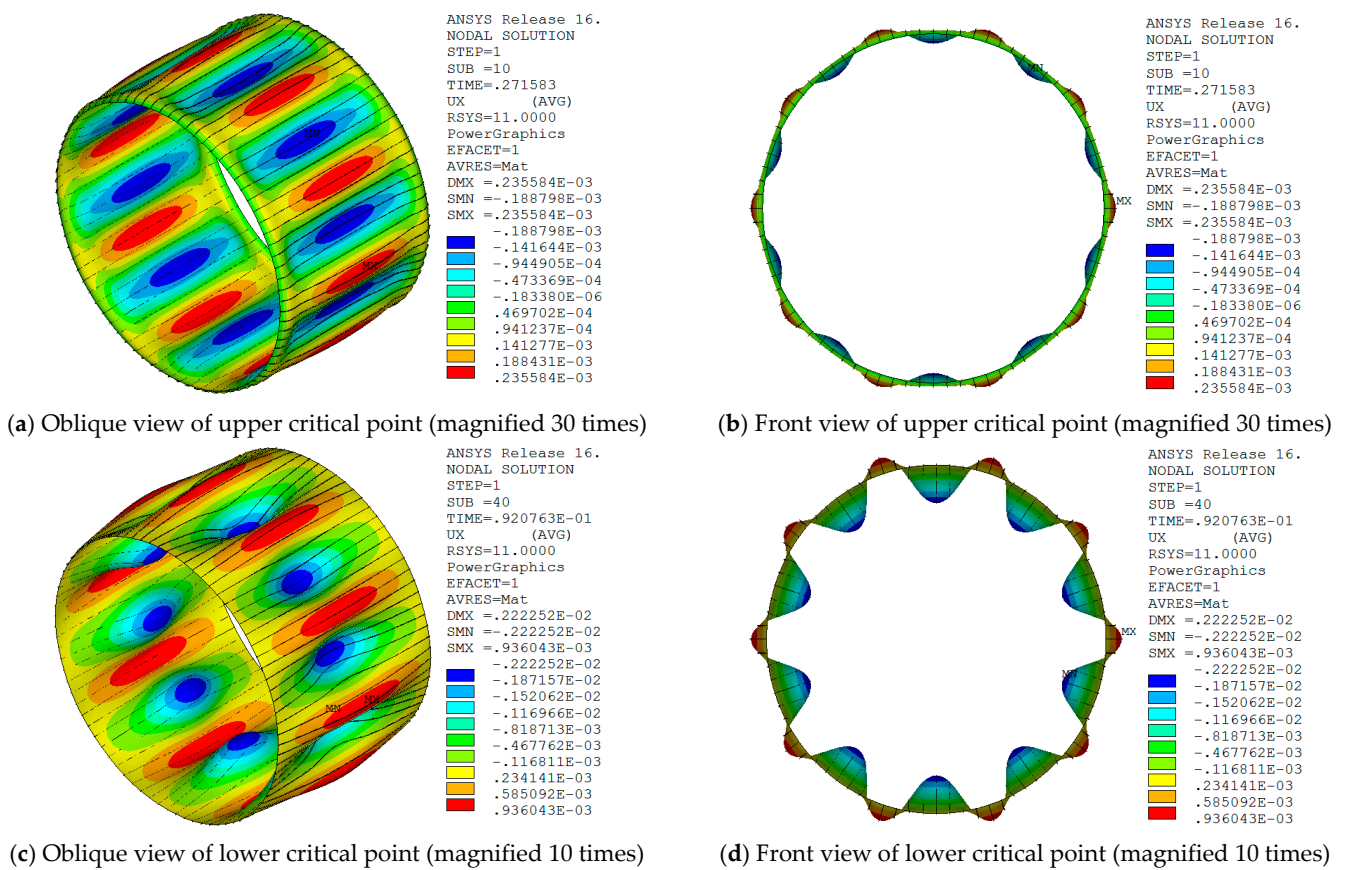


Figure 19. Radial displacement contour map at the critical points of the post-buckling path for the model with the SS3 boundary condition when the material of the model is PVC and  $\xi = 0.1$ .

### 5.3. Post-Buckling Similarity Simulation of Axial Compression Based on the DI

Parameters for the prototype of the LRRSC is shown in Table 8 [25]. Geometric scaling factors equal 10. The axial displacement constraint only is released at the upper boundary of the structure, and the fixed support is adopted at the lower boundary. The DI expressed by Equation (22,23) was introduced into the stiffened cylinders, and the center the DI is located at half the height of the structure.

**Table 8.** Geometric and material parameters of the LRRSC.

Material Parameters		Geometric Parameters of Skin				Stiffeners Parameters				
$E$ (GPa)	$\mu$	$L/m$	$R/m$	$t/m$	$L/R$	$h_s, h_r/mm$	$t_s, t_r/mm$	$N_s$	$N_r$	$R/t_{eff}$
72.40	0.3	6.0885	2.4257	0.0127	2.51	38.354	24.384	60	24	53.3421

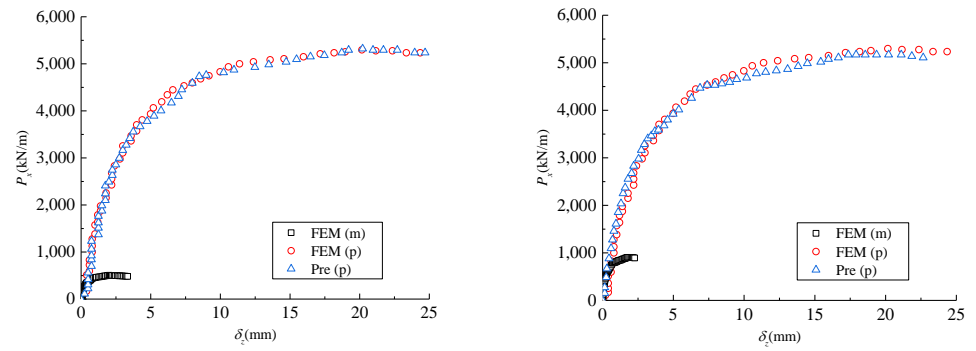
Taking the diameter of the DI equals to 0.060 m, with two imperfection amplitudes equal to  $0.1 \bar{t}$  and  $0.3 \bar{t}$ , respectively; the AR method was used to investigate the partial similitude of axial compression post-buckling of longitudinal-ring stiffened cylinders for the distorted scale models made of four materials.

It can be shown from Table 9 that, for the scaled models made of AL with two different imperfection amplitudes, the absolute relative error between the predicted prototypical buckling load by scaled models based on scaling law Equation (18) and the result of the prototype is within 2.00%. With the increase for deviation of Poisson's ratio between scaled models and the prototype, the relative error for buckling loads between the predicted prototype and the prototype is increased. When the scaled model material is PVC, the relative error between  $P_{xlim\_p\_pre}$  and  $P_{xlim\_p}$  achieves  $-8.83\%$ . The corresponding results can also be seen in the literature [25].

**Table 9.** Partial similitude simulation for post-buckling of LRRSC under axial compression.

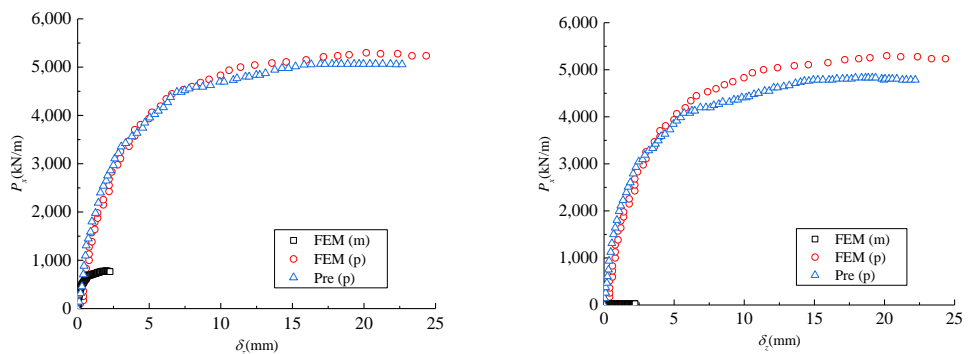
$\delta_0/m$	Material	Critical Buckling Load/ $kN \cdot m^{-1}$			Error/%
		Model	Prototype	Predicted Prototype	
$0.1 \bar{t}$	Al	595.318	6224.06	6269.24	0.73
$0.3 \bar{t}$		500.759	5273.95	5273.45	-0.01
$0.1 \bar{t}$	Copper	1055.31	6224.06	6033.68	-3.06
$0.3 \bar{t}$		898.381	5273.95	5136.44	-2.60
$0.1 \bar{t}$	Brass	900.281	6224.06	5976.10	-3.98
$0.3 \bar{t}$		767.129	5273.95	5092.24	-3.45
$0.1 \bar{t}$	PVC	32.182	6224.06	5674.80	-8.83
$0.3 \bar{t}$		27.270	5273.95	4808.64	-8.82

Figure 20 presents the load-displacement curves of four partial similitude scale models, the prototype and the corresponding prediction prototypes when the DI diameter is 0.060 m and the imperfection amplitude equals  $0.3 \bar{t}$ . Figure 21 shows the diagram of displacement vector at the points corresponding to the critical buckling loads of the prototype and four scale models made with distortion materials when the amplitude of imperfection equals  $0.3 \bar{t}$ . It can be found that, when the material of the scaled model is Al, the load-displacement curve of the predicted prototype can well agree with the result of the prototype; the error between  $P_{xlim\_p\_pre}$  and  $P_{xlim\_p}$  is  $-0.01\%$ ; the buckling modes of scaled models and the prototype at the buckling points are identical. With the increase for deviation of Poisson's ratio between the distorted scale model and the prototype, the deviation of load-displacement curves between the predicted prototype and the prototype is gradually increased. When the material of scale models is copper, brass and PVC, the errors between  $P_{xlim\_p\_pre}$  and  $P_{xlim\_p}$  are  $-2.60\%$ ,  $-3.45\%$ , and  $-8.82\%$ , respectively. The buckling mode shapes for scale models made of three different materials are consistent with the result of the prototype.



(a) The model material is AL

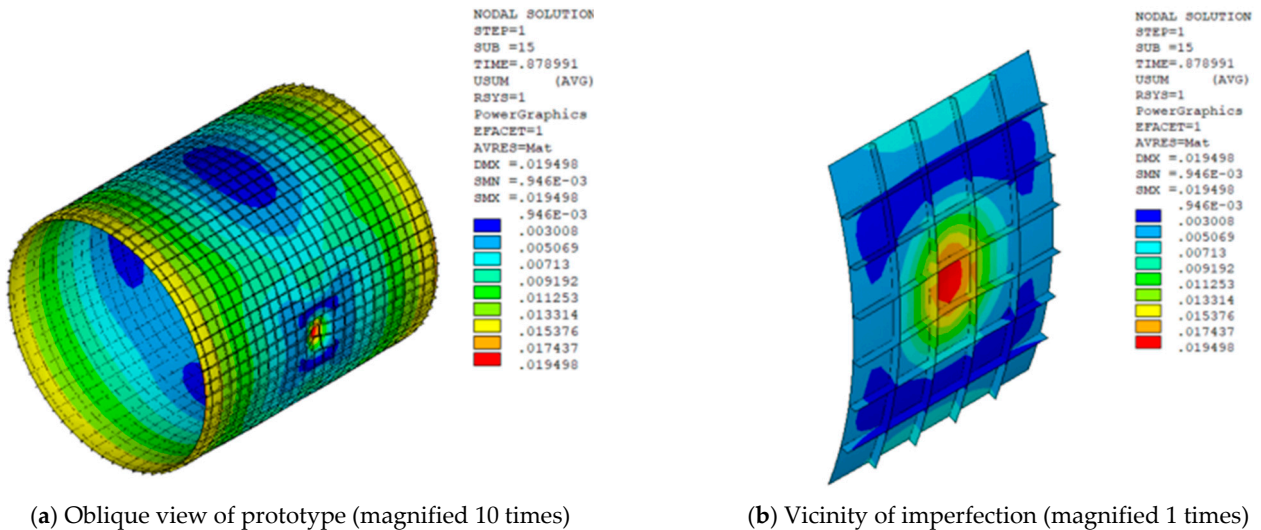
(b) The model material is copper



(c) The model material is brass

(d) The model material is PVC

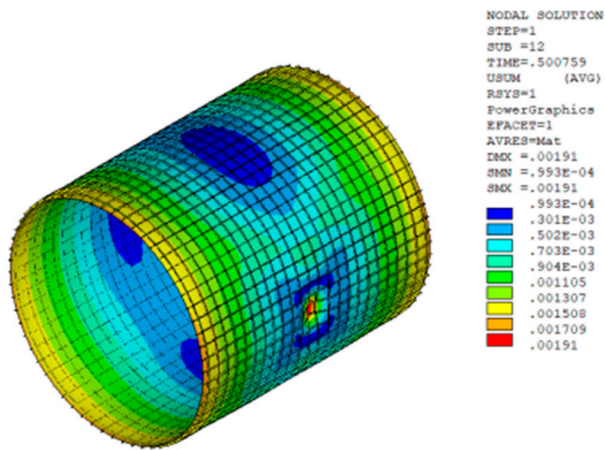
Figure 20. Comparison of partial similitude load-displacement curves for post-buckling of stiffened cylinders under axial compression when  $\delta_0 = 0.3 \bar{t}$ .



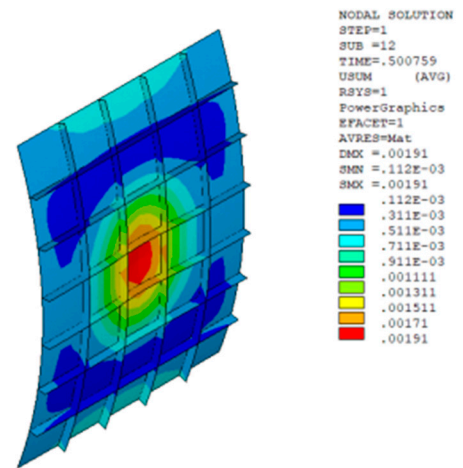
(a) Oblique view of prototype (magnified 10 times)

(b) Vicinity of imperfection (magnified 1 times)

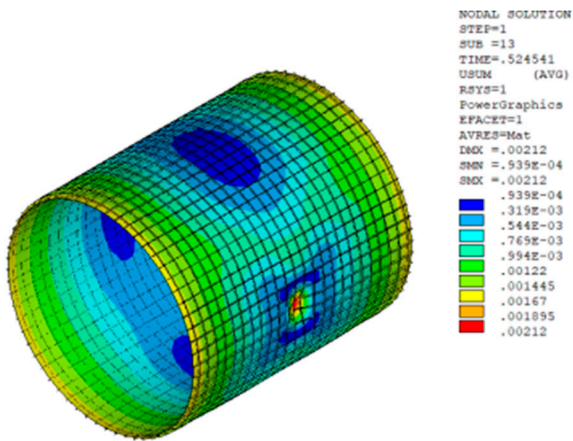
Figure 21. Cont.



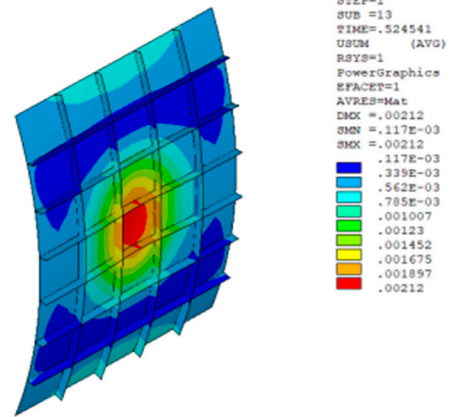
(c) Oblique view of AL model (magnified 10 times)



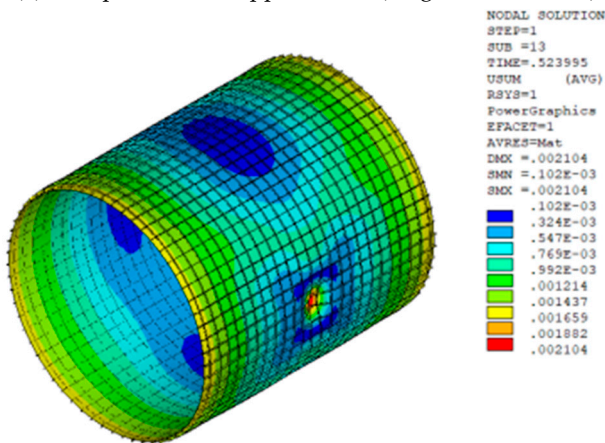
(d) Vicinity of imperfection (magnified 1 times)



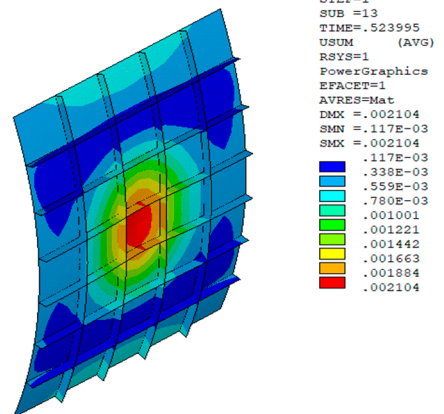
(e) Oblique view of copper model (magnified 10 times)



(f) Vicinity of imperfection (magnified 1 times)



(g) Oblique view of brass model (magnified 10 times)



(h) Vicinity of imperfection (magnified 1 times)

Figure 21. Cont.

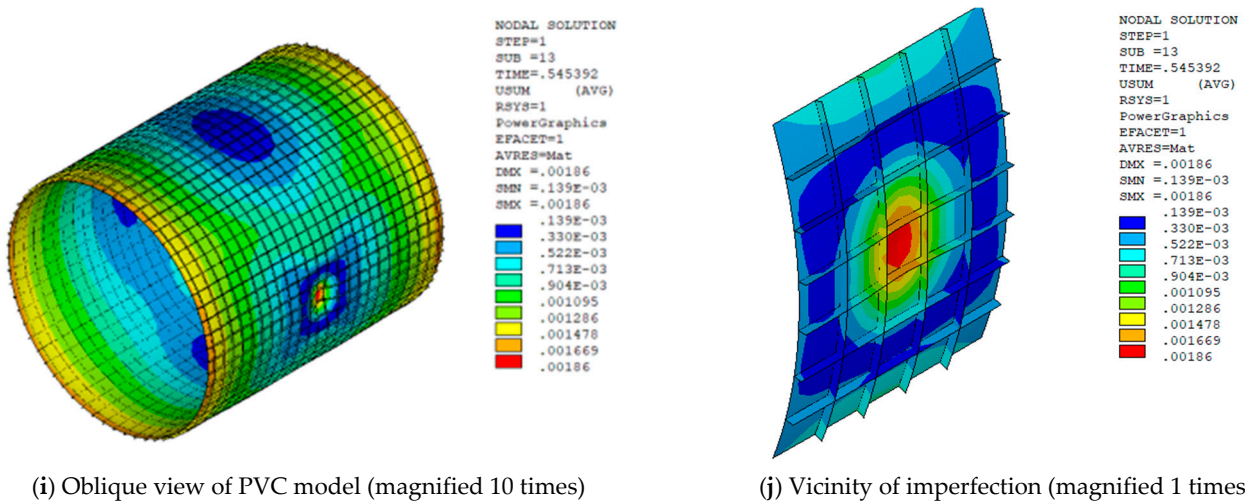


**Figure 21.** Comparison of buckling mode shapes between the prototype and distorted scale models when  $\lambda_m = 0.060$  m and  $\delta_0 = 0.3 \bar{t}$ .

5.4. Summary

When the material of scale models is distorted, normalized buckling load data  $P_{xlim\_p\_pre}/P_{xlim\_p}$  versus  $R/t_{eff}$  for stiffened cylinders with three different classes of initial geometrical imperfections and different imperfection factors are plotted in Figure 22. The analysis results indicated that the predicted axial compression buckling critical loads of stiffened cylinders with EMI, IDDI, or DI can agree well with the corresponding prototype results based on the derived scaling law. As the deviation of Poisson’s ratio of the scale models and prototype materials increases, the prediction accuracy between the buckling critical loads of prediction stiffened cylinders prototype and the results of the corresponding prototype under axial compression become more sensitive to the Poisson’s ratio. The derived general similitude conditions and the scaling laws are suitable for partial simulation of axial compression post-buckling of stiffened cylinders with different radius to effective thickness ratios.

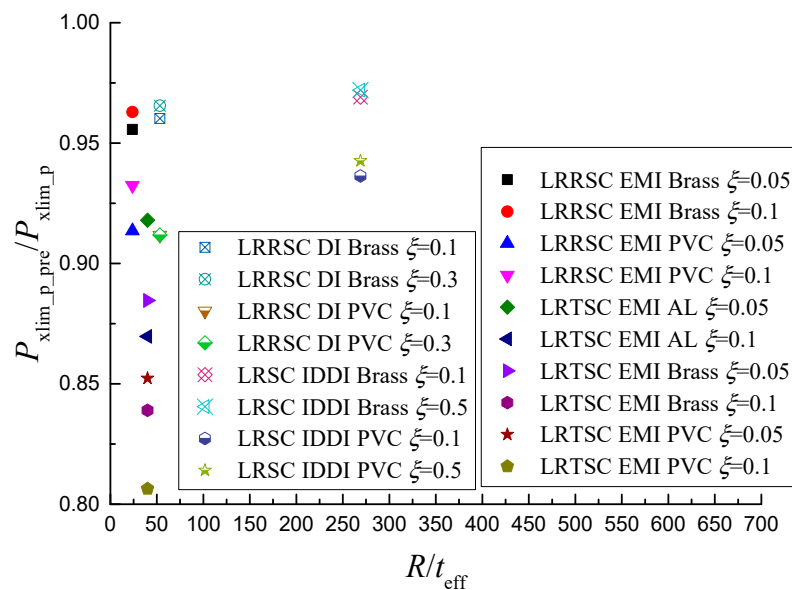


**Figure 22.**  $P_{xlim\_p\_pre}/P_{xlim\_p}$  versus  $R/t_{eff}$  for stiffened cylinders with initial geometrical imperfection.

## 6. Conclusions

This study investigated the applicability of small-scale distorted models in analyzing the post-buckling behavior of large longitudinal ring stiffened cylinders. Based on the Donnell nonlinear geometry equations with initial geometrical imperfections and the total energy of the structural system, the generalized similarity conditions and scaling laws were established for the axial compression post-buckling of the stiffened cylinders. Considering the EMI, IDDI, and DI, the partial similarities for axial compression post-buckling of the stiffened cylinders were investigated. The following conclusions were obtained:

(1) Partial similarity simulation results show that based on first-order EMI, the equilibrium paths of the scale models of longitudinal ring rectangular and T-type stiffened cylinders with SS3 or C3 boundary conditions under axial compression can well predict the results of the prototypes if the Poisson's ratio between the scale models and the corresponding prototype is equal. Based on the derived scaling law, the predicted axial compression post-buckling critical loads of stiffened cylinders can agree well with the prototypical results.

(2) Considering IDDI and DI, the equilibrium paths of the scale models of stiffened cylinders under axial compression can accurately predict the curves of the corresponding prototype if the Poisson's ratio between scale models and the prototype is equal. When the material of the models is brass or PVC, the equilibrium paths of scale models can predict the curves of the prototype, but the discrepancy between the predicted prototypical equilibrium paths and the results of the prototype under axial compression increases gradually with increasing deviation of the Poisson ratio between scale models and prototypical material.

(3) Parameter analysis shows that the proposed general similitude conditions and the scaling laws are suitable for similarity simulation of axial compression post-buckling of stiffened cylinders with radius to effective thickness ratios ranging from 23.76 to 268.95, rectangular or T-type stiffened cross-sections, EMI, IDDI, and DI, three type geometrical imperfections, and SS3 and C3, two type boundary conditions.

(4) The established general similarity conditions and the scaling laws were validated similarity numerically for axial compression post-buckling of longitudinal ring densely stiffened cylinders with geometric nonlinearity and initial geometric imperfections. These similarity relations for post buckling of stiffened cylinders can offer a valuable reference for scale model testing and buckling safety assessment of similar full-scale stiffened cylinders in practical engineering. Buckling scale distorted models of multi-stage stiffened cylinders will be studied in future.

**Author Contributions:** Conceptualization, W.Y. and W.Z.; methodology, W.Y.; software, S.D.; validation, S.D. and W.Y.; formal analysis, W.Y.; investigation, W.Y.; resources, W.Y. and W.Z.; data curation, S.D.; writing—original draft preparation, S.D.; writing—review and editing, W.Y. and C.Z.; visualization, S.D.; supervision, W.Y.; project administration, W.Y. and W.Z.; funding acquisition, W.Y. All authors have read and agreed to the published version of the manuscript.

**Funding:** This work is supported by the National Natural Science Foundation of China (51868013), Science and Technology Project of Guangxi (Guike AD19245127), Natural Science Foundation of Guangxi Province (2018GXNSFBA138056), Major science and technology projects of Guangxi (GuiKe AA18118008) and the Doctoral Research Initiation Fund of Guilin University of Technology (GUTQDJJ2017034). The authors are grateful for these financial supports.

**Institutional Review Board Statement:** Not applicable.

**Informed Consent Statement:** Not applicable.

**Data Availability Statement:** The data that support the findings of this study are available from the corresponding author upon reasonable request.

**Conflicts of Interest:** The authors declare no conflict of interest.

## References

1. Yu, W.; Li, Z. Structural similitude for prestressed vibration and buckling of eccentrically stiffened circular cylindrical panels and shells by energy approach. *Int. J. Struct. Stab. Dyn.* **2016**, *16*, 1550074. [\[CrossRef\]](#)
2. Ezra, A.A. *Similitude Requirements for Scale Model Determination of Shell Buckling under Impulsive Pressure*; Technical Report 19630000981; NTRS-NASA: Washington, DC, USA, 1962.
3. Morgan, G.W. Scaling techniques for orthotropic cylindrical aerospace structures. In Proceedings of the AIAA 5th Annual Structures and Materials Conference, Palm Spring, CA, USA, 1–3 April 1964; pp. 333–343.
4. Ni, H. Strength and Stability Analyses for Sphere-Toroid-Cone Rotational Shells. Ph.D. Thesis, China Ship Development & Design Center, Wuhan, China, 2012.
5. Simitse, G.J.; Rezaeepazhand, J. Structural similitude and scaling laws for buckling of cross-ply laminated plates. *J. Thermoplast. Compos. Mater.* **1995**, *8*, 240–251. [\[CrossRef\]](#)
6. Rezaeepazhand, J.; Simitse, G.J.; Starnes, J.H., Jr. Scale models for laminated cylindrical shells subjected to axial compression. *Compos. Struct.* **1996**, *34*, 371–379. [\[CrossRef\]](#)
7. Simitse, G.J.; Rezaeepazhand, J.; Sierakowski, R.L. Scaled models for laminated cylindrical shells subjected to external pressure. *Mech. Compos. Mater. Struct.* **1997**, *4*, 267–280. [\[CrossRef\]](#)
8. Simitse, G.J. Structural similitude for flat laminated surfaces. *Compos. Struct.* **2001**, *51*, 191–194. [\[CrossRef\]](#)
9. Simitse, G.J.; Rezaeepazhand, J. Structural similitude for laminated structures. *Compos. Eng.* **1993**, *3*, 751–765. [\[CrossRef\]](#)
10. Rezaeepazhand, J.; Simitse, G.J.; Starnes, J.H., Jr. Design of scaled down models for predicting shell vibration response. *J. Sound Vib.* **1996**, *195*, 301–311. [\[CrossRef\]](#)
11. Frostig, Y.; Simitse, G.J. Similitude of sandwich panels with a ‘soft’ core in buckling. *Compos. Part B* **2004**, *35*, 599–608. [\[CrossRef\]](#)
12. Ungbhakorn, V.; Singhatanadgid, P. Scaling law and physical similitude for buckling and vibration of antisymmetric angle-ply laminated cylindrical shells. *Int. J. Struct. Stab. Dyn.* **2003**, *3*, 567–583. [\[CrossRef\]](#)
13. Ungbhakorn, V.; Singhatanadgid, P. Similitude and physical modeling for buckling and vibration of symmetric cross-ply laminated circular cylindrical shells. *J. Compos. Mater.* **2003**, *37*, 1697–1712. [\[CrossRef\]](#)
14. Ungbhakorn, V.; Singhatanadgid, P. Similitude invariants and scaling laws for buckling experiments on anti-symmetrically laminated plates subjected to biaxial loading. *Compos. Struct.* **2003**, *59*, 455–465. [\[CrossRef\]](#)
15. Singhatanadgid, P.; Ungbhakorn, V. Scaling laws for buckling of polar orthotropic annular plates subjected to loading. *Thin-Walled Struct.* **2005**, *43*, 1115–1129. [\[CrossRef\]](#)
16. Rezaeepazhand, J.; Wisnom, M.R. Scaled models for predicting buckling of delaminated orthotropic beam-plates. *Compos. Struct.* **2009**, *90*, 87–91. [\[CrossRef\]](#)
17. Shokrieh, M.M.; Askari, A. Similitude study of impacted composite laminates under buckling loading. *J. Eng. Mech.* **2013**, *139*, 1334–1340. [\[CrossRef\]](#)
18. Rudd, M.T.; Schultz, M.R.; Waters, W.A.; Gardner, N.W.; Bisagni, C. Buckling testing of a subscale composite cylinder. In Proceedings of the AIAA Scitech 2021 Forum, Virtual/online event, 11–15 & 19–21 January 2021; pp. 1–12. [\[CrossRef\]](#)
19. Eberlein, D.J. Composite Cylindrical Shell Buckling Simulation & Experimental Correlation. Master’s Thesis, Delft University of Technology, Delft, The Netherlands, 2019.
20. Balbin, I.U.; Bisagni, C.; Schultz, M.R.; Hilburger, M.W. Scaling methodology applied to buckling of sandwich composite cylindrical shells. *AIAA J.* **2020**, *58*, 3680–3689. [\[CrossRef\]](#)
21. Przekop, A.; Schultz, M.R.; Hilburger, M.W. Design of buckling-critical large-scale sandwich composite cylinder test articles. In Proceedings of the AIAA/ASCE/AHS/ASC Structures, Structural Dynamics, and Materials Conference, Kissimmee, FL, USA, 8–12 January 2018; pp. 1–23.
22. Kasivitanuay, J.; Singhatanadgid, P. Application of an energy theorem to derive a scaling law for structural behaviors. *Thammasat Int. J. Sc.Tech* **2005**, *10*, 33–40.
23. Ungbhakorn, V.; Singhatanadgid, P. A Scaling law for vibration response of laminated doubly curved shallow shells by energy approach. *Mech. Adv. Mater. Struct.* **2009**, *16*, 333–344. [\[CrossRef\]](#)
24. Kasivitanuay, J.; Singhatanadgid, P. Scaling laws for displacement of elastic beam by energy method. *Int. J. Mech. Sci.* **2017**, *128–129*, 361–367. [\[CrossRef\]](#)
25. Jiawei, D.; Xinkui, X.; Wei, Y.; Zhu, W. Study on the axial compression postbuckling similitude model of the stiffened cylindrical shell with dimple imperfections. *Adv. Civ. Eng.* **2021**, *2021*, 6637891.
26. Zhengliang, L.; Jingchao, W.; Wei, Y.; Wanxu, Z. Study on post-buckling scale model of stringer stiffened-cylindrical shells under axial compression based on discrete stiffened method. *J. Hunan Univ. Nat. Sci.* **2022**, *49*, 123–132.
27. Zhengliang, L.; Jingchao, W.; Wei, Y. Structural similitude for nonlinear buckling of discrete orthogonally stiffened cylindrical shells subjected to external pressure by energy approach. *Int. J. Struct. Stab. Dyn.* **2022**, *22*, 2240021.
28. Kasivitanuay, J.; Singhatanadgid, P. Scaling laws for static displacement of linearly elastic cracked beam by energy method. *Theor. Appl. Fract. Mech.* **2018**, *98*, 157–166. [\[CrossRef\]](#)
29. Lilin, Z. Energy similitude correction method for free vibration of cylinders. *Int. J. Struct. Stab. Dyn.* **2021**, *21*, 2150023.
30. Lilin, Z. A new structural similitude method for laminated composite cylinders. *Thin-Walled Struct.* **2021**, *164*, 107920.
31. Lilin, Z. A novel similitude method for predicting natural frequency of FG porous plates under thermal environment. *Mech. Adv. Mater. Struct.* **2021**, 1–17. [\[CrossRef\]](#)

32. Lilin, Z. Similitude analysis of free vibration of functionally graded material cylinders under thermal environment. *Mech. Syst. Signal Process.* **2022**, *170*, 108821.
33. Thornburgh, R.P.; Hilburger, M.W. *Design of Orthogrid Cylinder Test Articles for the Shell Buckling Knockdown Factor Assessment*; Technical Report NASA/TM-2010-216866; NASA: Washington, DC, USA, 2010.
34. Hilburger, M.W.; Haynie, W.T.; Lovejoy, A.E.; Roberts, M.G.; Norris, J.P.; Waters, W.A.; Herring, H.M. Subscale and full-scale testing of buckling-critical launch vehicle shell structures. In Proceedings of the 53rd AIAA/ASME/ASCE/AHS/ASC Structures, Structural Dynamics, and Materials Conference, Honolulu, HI, USA, 23–26 April 2012; pp. 1–33.
35. Hilburger, M.W.; Lovejoy, A.E.; Thornburgh, R.P.; Rankin, C. Design and analysis of subscale and full-scale buckling-critical cylinders for launch vehicle technology development. In Proceedings of the 53rd AIAA/ASME/ASCE/AHS/ASC Structures, Structural Dynamics, and Materials Conference, Honolulu, HI, USA, 23–26 April 2012; pp. 1–48.
36. Wang, B.; Du, K.; Hao, P.; Zhou, C.; Tian, K.; Xu, S.; Ma, Y.; Zhang, X. Numerically and experimentally predicted knockdown factors for stiffened shells under axial compression. *Thin-Walled Struct.* **2016**, *109*, 13–24. [[CrossRef](#)]
37. Hilburger, M.W. On the development of shell buckling knockdown factors for stiffened metallic launch vehicle cylinders. In Proceedings of the AIAA/ASCE/AHS/ASC Structures, Structural Dynamics, and Materials Conference, Kissimmee, FL, USA, 8–12 January 2018; pp. 1–17.
38. Brush, D.O.; Almroth, B.O. *Buckling of Bars, Plates, and Shells*; McGraw-Hill: New York, NY, USA, 1975; pp. 177–178.
39. Amabili, M. *Nonlinear Vibrations and Stability of Shells and Plates*; Cambridge University Press: New York, NY, USA, 2008; pp. 29–32.
40. Ventsel, E.; Krauthammer, T. *Thin Plates and Shells: Theory, Analysis, and Applications*; Marcel Dekker: New York, NY, USA, 2001; p. 548.
41. Lianyuan, W. *Theory of Plate and Shell Stability*; Huazhong University of Science and Technology Press: Wuhan, China, 1996; p. 236.
42. Crisfield, M.A. A fast incremental iterative solution procedure that handles “snap-through”. *Comput. Struct.* **1981**, *13*, 55–62. [[CrossRef](#)]
43. Narayana, Y.V.; Gunda, J.B.; Reddy, P.R.; Markandeya, R. Nonlinear buckling and post-buckling analysis of imperfect cylindrical shells subjected to axial compressive load. *J. Struct. Eng.* **2015**, *42*, 78–85.
44. Arbocz, J.; Sechler, E.E. On the buckling of stiffened imperfect cylindrical shells. *AIAA J.* **1976**, *14*, 1611–1617. [[CrossRef](#)]
45. Arbocz, J. Post-buckling behavior of structures numerical techniques for more complicated structures. In *Buckling and Post-buckling*; The series Lecture Notes in Physics; Araki, H., Ehlers, J., Hepp, K., Kippenhahn, R., Weidebnüller, H.A., Wess, J., Zittartz, J., Eds.; Springer: Berlin/Heidelberg, Germany, 2005; Volume 288, pp. 83–142.
46. Bo, W.; Peng, H.; Gang, L.; Yaochu, F.; Xiaojun, W.; Xi, Z. Determination of realistic worst imperfection for cylindrical shells using surrogate model. *Struct. Multidiscip. Optim.* **2013**, *45*, 777–794.
47. Meyer-Piening, H.R.; Farshad, M.; Geier, B.; Zimmermann, R. Buckling loads of CFRP composite cylinders under combined axial and torsion loading-experiment and computations. *Compos. Struct.* **2001**, *53*, 427–435. [[CrossRef](#)]
48. Simitse, G.J. Buckling and post buckling of imperfect cylindrical shells: A review. *Appl. Mech. Rev.* **1986**, *39*, 1517–1524. [[CrossRef](#)]